Am J Cancer Res 2026;16(11):4733-4755
www.ajcr.us /ISSN:2156-6976/ajcr0175120

Original Article

Elevated SMC1B promotes prostate cancer aggressiveness in epithelial cells: an integrated MR, single-cell, and experimental study

Yunfeng Gao[1,2], Xueyang He[2], Chaoyou Huang[2], Weiyang He[1]

[1]*Department of Urology, The First Affiliated Hospital of Chongqing Medical University, Chongqing 400016, China;* [2]*Department of Urology, Chengdu Second People's Hospital, Chengdu 610000, Sichuan, China*

Received July 2, 2026; Accepted October 20, 2026; Epub November 15, 2026; Published November 30, 2026

Abstract: Prostate cancer (PRAD) remains a leading male malignancy with high incidence and mortality. Although SMC1B participates in DNA repair and cell-cycle regulation, its causal role, molecular mechanisms, and clinical significance in PRAD remain unclear. To elucidate these aspects, we integrated bioinformatics, Mendelian randomization (MR), and experimental validation: two-sample MR was performed using FinnGen R12 PRAD GWAS data (20,368 cases/156,671 controls) and SMC1B expression quantitative trait loci (eQTL) data from OpenGWAS to test causal direction; TCGA-PRAD (n = 548) and GSE176031 single-cell data (4 tumor/4 control) were used for differential expression, Weighted gene co-expression network analysis, Cox regression, nomogram construction, functional enrichment, and CellChat-based intercellular communication analysis; SMC1B expression was validated in paired clinical PRAD specimens by qRT-PCR, Western blot, and IHC; and siRNA-mediated SMC1B knockdown was performed in PC-3 and LNCaP cells, followed by CCK-8, colony formation, wound-healing, Transwell, flow-cytometric cell-cycle and apoptosis assays, immunoblotting of γH2AX/RAD51 and the BRCA1-PALB2-BRCA2-RAD51 HR mediator axis, and an enzalutamide-based AR blockade experiment. MR confirmed a robust causal relationship between elevated SMC1B expression and increased PRAD risk (IVW $P < 0.05$; consistent across MR-Egger, weighted-median, and weighted-mode estimators; no horizontal pleiotropy or heterogeneity). SMC1B was significantly up-regulated in tumor versus paired normal tissues at mRNA, protein, and immunohistochemical levels ($P < 0.001$), and high SMC1B expression independently predicted shorter overall survival (HR = 1.75, 95% CI: 1.15-2.66, $P = 0.009$). WGCNA identified 1,970 SMC1B-co-expressed genes enriched in homologous recombination, Fanconi anemia, and DNA-replication fidelity pathways, while single-cell analysis localized the SMC1B functional gene set predominantly to malignant epithelial cells, which exhibited the strongest CellChat-inferred signaling with basal, endothelial, and T cells via HBEGF-EGFR, VEGFA-VEGFR, APP-CD74, JAG1-NOTCH2, and COL1A1-ITGA1-ITGB1 axes. In both PC-3 and LNCaP cells, siRNA-mediated SMC1B knockdown elevated γH2AX, coordinately down-regulated the BRCA1-PALB2-BRCA2-RAD51 HR mediator axis at both transcriptional and protein levels, suppressed proliferation, clonogenicity, migration, and invasion, induced G0/G1 arrest with concurrent S-phase reduction, and increased apoptosis. Two-way ANOVA of combined SMC1B knockdown and enzalutamide treatment revealed that SMC1B-mediated perturbation of HR mediators operates independently of AR signaling. Collectively, these integrated causal, cell-type-resolved, and in vitro data indicate that elevated SMC1B expression is associated with aggressive PRAD phenotypes and coordinated perturbation of the BRCA1-PALB2-BRCA2-RAD51 HR mediator axis in malignant epithelial cells independently of AR status, suggesting that SMC1B represents a candidate prognostic biomarker that warrants further validation in prospective cohorts and direct in vivo functional investigation before clinical translation.

Keywords: Prostate cancer, SMC1B, Mendelian randomization, single-cell RNA sequencing, tumor microenvironment, experimental validation

Introduction

Prostate cancer (PRAD) is one of the most common malignant tumors in men worldwide, ranking second in incidence and fifth in mortality among male cancers [1, 2]. In 2020, approximately 1.4 million new cases of PRAD and over 370,000 deaths were reported globally [3]. Although prostate-specific antigen (PSA) screening, radical prostatectomy, and androgen

https://doi.org/10.62347/HBHH4811

deprivation therapy have significantly improved the prognosis of patients with early-stage PRAD, approximately 20-30% of patients experience biochemical recurrence after initial treatment, with some eventually progressing to metastatic castration-resistant PRAD (mCRPC) [4, 5]. The 5-year survival rate for mCRPC patients is less than 30%, with an extremely poor prognosis [6]. Therefore, in-depth exploration of the molecular mechanisms underlying PRAD development and progression, and identification of novel diagnostic biomarkers are of great clinical significance.

The structural maintenance of chromosomes (SMC) protein family comprises highly conserved ATPases in eukaryotes that play crucial roles in chromosome structure maintenance, DNA repair, and gene expression regulation [7]. SMC1B is an important member of the SMC family, primarily participating in sister chromatid cohesion and homologous recombination during meiosis [8]. Recent studies have revealed that SMC1B is aberrantly expressed in various malignant tumors and is involved in tumor progression. Li et al. found that SMC1B promotes cervical squamous cell carcinoma progression through the PI3K/Akt pathway [9]. Furthermore, in colorectal tumors, particularly in the development of traditional serrated adenomas (TSA), SMC1B plays an important role through epigenetic silencing (such as DNA methylation) and may serve as a diagnostic marker for TSA, associated with KRAS mutations and the CpG island methylator phenotype (CIMP) [10]. Importantly, although SMC1B was historically considered a meiosis-specific cohesin subunit, recent evidence has unequivocally demonstrated its expression and function in somatic mammalian cells, where it participates in mitotic cohesin complexes and safeguards genome stability following DNA damage [11]. This emerging dual role suggests that SMC1B aberrant up-regulation in solid tumors - including PRAD - may confer a survival advantage by reinforcing DNA damage repair, particularly homologous recombination (HR), thereby providing both a mechanistic rationale for studying SMC1B in PRAD and a possible translational direction worthy of further mechanistic investigation. However, direct in vitro evidence linking SMC1B to HR-dependent phenotypes in PRAD cells has been lacking, motivating the integrated MR, multi-omics, and functional validation strategy adopted in the present study.

Traditional observational studies are susceptible to confounding factors and reverse causality, making it difficult to accurately assess the causal relationship between gene expression and disease risk [12]. Mendelian randomization (MR) analysis uses genetic variants as instrumental variables and, based on the principle of random gene allocation, can effectively avoid confounding bias in traditional epidemiological studies, providing reliable evidence for causal inference [13, 14]. In recent years, MR methods have been widely applied in tumor etiology research, successfully revealing causal relationships between multiple gene expressions and cancer risk [15, 16]. However, there is currently a lack of studies systematically evaluating the causal relationship between SMC1B and PRAD using MR methods.

Single-cell RNA sequencing (scRNA-seq) enables precise identification of cell types in the tumor microenvironment and analysis of functional characteristics and interactions of different cell subpopulations through transcriptomic analysis at single-cell resolution [17]. In PRAD research, scRNA-seq has successfully revealed clonal evolution of tumor cells, immune evasion mechanisms, and the cellular basis of therapeutic resistance [18, 19].

Based on the above background, this study aims to systematically elucidate the causal role, molecular mechanisms, and clinical value of SMC1B in PRAD through integrated Mendelian randomization analysis, large-scale transcriptomic data mining, single-cell transcriptome analysis and experimental validation. This study will provide comprehensive evidence for in-depth understanding of the role of SMC1B in PRAD and to provide a mechanistic foundation for future translational investigation.

Methods

Data download and preprocessing

The PRAD-related transcriptome dataset GSE176031 was downloaded from the Gene Expression Omnibus (GEO) database (https://www.ncbi.nlm.nih.gov/geo/). The GSE176031 dataset is based on the GPL11154 platform

and includes single-cell sequencing data from 4 tumor samples and 4 normal control samples.

Gene expression data from TCGA-PRAD were downloaded from The Cancer Genome Atlas (TCGA) (https://portal.gdc.cancer.gov/), containing 496 cancer samples and 52 control samples.

Genome-wide association study (GWAS) summary statistics for PRAD were retrieved from the FinnGen consortium R12 release (phenotype code: C3_PROSTATE_EXALLC), comprising 20,368 cases and 156,671 controls of European ancestry (total N = 177,039). Cis-expression quantitative trait loci (cis-eQTL) summary data for SMC1B (Ensembl ID: ENSG00000077935; OpenGWAS ID: eqtl-a-ENSG00000077935) were obtained from the eQTLGen consortium via the IEU OpenGWAS platform. This expression quantitative trait loci (eQTL) dataset is derived from peripheral blood samples of up to 31,684 European individuals based on high-throughput transcriptome profiling and dense genotyping platforms. Both datasets were aligned to the human genome build GRCh37/hg19.

Mendelian randomization analysis

Two-sample Mendelian randomization (MR) analysis was performed using the TwoSampleMR package (v0.6.7) to evaluate the causal relationship between genetically predicted SMC1B expression and PRAD risk. Instrumental single nucleotide polymorphisms (SNPs) for SMC1B were selected using a genome-wide significance threshold of $P < 5 \times 10^{-8}$. To ensure instrument independence, linkage disequilibrium (LD) clumping was applied based on the 1000 Genomes European reference panel with strict criteria of $r^2 < 0.001$ and a clumping window of > 10,000 kb. Palindromic SNPs with intermediate allele frequencies and incompatible alleles were excluded during harmonization. The strength of each instrumental variable was evaluated using the F-statistic ($F = Beta^2/SE^2$), where F > 10 indicated the absence of weak instrument bias.

The random-effects inverse-variance weighted (IVW) method was utilized as the primary analysis, supplemented by MR-Egger, weighted median, simple mode, and weighted mode estimators. Heterogeneity among instruments was assessed via Cochran's Q test (P > 0.05 indicating absence of heterogeneity). Potential horizontal pleiotropy was evaluated using the MR-Egger intercept test (P > 0.05 indicating no directional pleiotropy). In addition, leave-one-out sensitivity analyses and funnel plots were generated to assess whether the causal estimate was driven by any single outlying SNP.

SMC1B co-expressed gene acquisition and prognostic analysis

Based on the TCGA-PRAD dataset, differential expression analysis and univariate/multivariate Cox regression of SMC1B were performed. Patients were stratified by median SMC1B expression. Kaplan-Meier (KM) survival curves with log-rank test compared overall survival (OS), and time-dependent receiver operating characteristic (ROC) curves evaluated predictive efficacy. Before establishing the multivariable model, the proportional hazards assumption was verified using the Schoenfeld residuals test (cox.zph function, survival package); non-significant departure (P > 0.05) confirmed the validity of the proportional hazards assumption. A nomogram integrating SMC1B expression, age, and T stage was then constructed with Bootstrap resampling (1,000 iterations) to generate calibration curves assessing predictive performance. Decision curve analysis (DCA) evaluated clinical net benefit.

Differentially expressed genes (DEGs) were screened using the limma package with Benjamini-Hochberg (BH) false discovery rate (FDR) adjusted P < 0.05 and |log2 fold change| > 0.25. For clinical prognostic modeling, a complete-case analysis strategy was implemented by removing cases with missing clinical stages or incomplete survival follow-up data prior to analysis, ensuring that all patients entered into the Cox regression and nomogram had complete information. Weighted gene co-expression network analysis (WGCNA) constructed co-expression networks (soft threshold β = 5, minimum module size = 40 genes). Hub genes within modules were identified using dual criteria (module membership [MM] > 0.8), yielding candidate genes.

Functional enrichment analysis

The DAVID database was used for Gene Ontology (GO) and Kyoto Encyclopedia of Genes and Genomes (KEGG) pathway enrichment analyses, with significance defined by BH adjusted $P < 0.05$. Gene Set Enrichment Analysis (GSEA) was performed to evaluate signaling differences between the SMC1B high and low expression groups, with pathways showing normalized enrichment score $|NES| > 1$ and FDR q-value < 0.05 (adjusted $P < 0.05$) considered significantly enriched.

Single-cell transcriptome analysis

Based on the GSE176031 dataset, Seurat (v5.1.0) performed quality control (nFeature_RNA > 200 & < 5,000 & percent.mt < 20%), normalization, feature selection (2,000 highly variable genes), and Principal Component Analysis (PCA) dimensionality reduction. To remove technical batch effects across the eight independent clinical specimens (4 tumor and 4 normal samples) while preserving genuine biological heterogeneity, batch correction was performed on the top 30 principal components using the Harmony R package (v1.2.3), with the sample identifier (orig.ident) specified as the batch variable. After correction, cells from different specimens were well intermixed within biologically meaningful clusters. Cells were clustered using Shared Nearest Neighbor (SNN) graphs and Louvain algorithm, with cell-type annotation based on CellMarker database marker genes and Uniform Manifold Approximation and Projection (UMAP) visualization.

The SMC1B-related gene set was obtained by intersecting single-cell differential genes with SMC1B co-expressed genes. Three independent scoring methods (AUCell, PercentageFeatureSet, and ssGSEA) evaluated enrichment characteristics. Single-cell differential expression was analysed with Wilcoxon rank-sum test. Multiple testing was corrected via BH-FDR (adj.P < 0.05). Enrichment score comparisons across cell types were tested with Wilcoxon rank-sum test followed by BH correction.

CellChat (v1.6.1) was used to identify significant ligand-receptor pairs mediating intercellular communication, based on the CellChatDB. human curated database. Communication probability was calculated using the trimean method. Interactions with $P < 0.05$ (permutation test, 100 iterations) were retained. Pairs were categorised into secreted-signalling, ECM-receptor, and cell-cell-contact classes.

Clinical sample experiments and cell experiments for verification

Clinical specimens: PRAD and adjacent non-tumor tissues were collected from patients undergoing radical prostatectomy. Fresh-frozen tissues with well-preserved RNA (3 pairs) were used for qRT-PCR, and those with qualified protein (3 pairs) for Western blot and immunohistochemistry (IHC). These three paired specimens were used for preliminary exploratory validation of the bioinformatic findings. All samples were obtained with written informed consent under institutional ethics committee approval. This study was conducted in accordance with the Declaration of Helsinki and approved by the Medical Ethics Committee of Chengdu Second People's Hospital (approval number [KY]PJ202658).

Cell culture and siRNA transfection: PC-3 and LNCaP human PRAD cell lines were maintained at 37°C with 5% CO_2. For loss-of-function studies, cells were transfected with SMC1B-targeting siRNA (si-SMC1B) or negative-control siRNA (si-NC) according to the manufacturer's instructions, generating PC-3/siNC, PC-3/siSMC1B, LNCaP/siNC, and LNCaP/siSMC1B groups. Cells were harvested 48 h post-transfection for downstream analyses.

Quantitative real-time PCR (qRT-PCR): Reverse transcription was performed in 20 µL reactions containing 1 µg total RNA, 4 µL 5× PrimeScript Buffer, 1 µL PrimeScript RT Enzyme Mix I, 1 µL Oligo dT primer (50 µM), 1 µL Random 6-mers (100 µM), and RNase-free water; the thermal profile was 37°C/15 min followed by 85°C/5 s. Real-time qPCR was performed in 20 µL reactions containing 10 µL 2× TB Green Premix Ex Taq II, 0.8 µL each of forward and reverse primer (10 µM), 2 µL cDNA template, and 6.4 µL RNase-free water. Thermal cycling: initial denaturation 95°C/30 s; 40 cycles of 95°C/5 s and 60°C/30 s; melt curve 65°C→95°C in 0.5°C increments. All reactions were run in technical triplicate on a Bio-Rad CFX96 system. Relative expression

was calculated by the $2^{-\Delta\Delta Ct}$ method with GAPDH as the internal reference. Primer sequences are listed in Supplementary Table 1.

Western blot: Tissues were homogenized in RIPA lysis buffer (Beyotime, P0013C) supplemented with protease and phosphatase inhibitors; cells were lysed directly on ice. Protein concentration was determined by BCA assay (Epizyme Biotech, ZJ101L). Equal amounts of protein (20 μg/lane) were resolved on 4-20% gradient SDS-PAGE gels and transferred to PVDF membranes (Millipore). After blocking and overnight primary antibody incubation at 4°C, membranes were probed with HRP-conjugated secondary antibody and signals detected by ECL chemiluminescence. Band intensities were quantified with ImageJ and normalized to GAPDH. Membranes were incubated overnight at 4°C with the following primary antibodies: SMC1B (Thermo Fisher, PA5-22199, 1:1,000; Akmaijie, PSI-57-308, 1:200 for IHC), γH2AX (Proteintech, 83307-2-RR, 1:1,000), RAD51 (Proteintech, 14961-1-AP, 1:1,000), BRCA1 (Proteintech, 22362-1-AP, 1:1,000), PALB2 (Abcam, ab202970, 1:1,000), BRCA2 (Proteintech, 19791-1-AP, 1:1,000), AR (CST, 5153S, 1:1,000), PSA (CST, 5365S, 1:1,000), and GAPDH (ABclonal, A19056, 1:5,000), followed by HRP-conjugated secondary antibodies (ABclonal, AS014 for anti-rabbit and AS003 for anti-mouse, 1:5,000).

Immunohistochemistry (IHC): FFPE prostate tissue sections were deparaffinized, rehydrated, and subjected to microwave antigen retrieval in citrate buffer (pH 6.0). Endogenous peroxidase was quenched with 3% H_2O_2, and sections were blocked with 3% BSA before overnight incubation at 4°C with anti-SMC1B antibody (Akmaijie, PSI-57-308). After species-matched secondary antibody incubation, signal was developed with DAB and nuclei were counterstained with hematoxylin. Positive staining appeared brown/yellow-brown. Images were acquired at ×400 magnification using a Nikon ECLIPSE Ni-U microscope with a Nikon DS-Ri2 digital camera.

CCK-8 cell proliferation assay: Transfected cells were seeded into 96-well plates (~5×10^3 cells/well). CCK-8 reagent (Dojindo, CK04) was added at 0, 24, 48, and 72 h, and absorbance at 450 nm was recorded after 4 h incubation.

Colony formation assay: Transfected cells (800/well) were seeded into 12-well plates and cultured until colonies reached ~50 cells. Colonies were fixed with 4% paraformaldehyde and stained with 0.1% crystal violet. Colony numbers were quantified using ImageJ.

Wound-healing assay: Transfected cells were seeded to confluence in 6-well plates and a linear scratch was introduced with a pipette tip. Images were captured at 0 and 24 h. Migration area (%) was calculated as [(initial wound area - residual wound area)/initial wound area] × 100%.

Transwell invasion assay: Matrigel-coated Transwell inserts (Corning, 3422) were prepared according to the manufacturer's instructions. Transfected cells (2×10^4) in serum-free medium were seeded into the upper chamber, with 20% FBS medium in the lower chamber as chemoattractant. After 24-48 h, non-invading cells were removed; invaded cells were fixed, stained with crystal violet, and counted in five random fields.

Flow-cytometric apoptosis analysis: Transfected cells were stained with Annexin V-FITC and propidium iodide (PI) using the Beyotime kit (C1062S) and analyzed by flow cytometry. The apoptosis rate was defined as the sum of early (Annexin V^+/PI^-) and late apoptotic (Annexin V^+/PI^+) populations.

Flow-cytometric cell-cycle analysis: Transfected cells were fixed in 70% ethanol at 4°C, washed, and stained with PI solution (Beyotime, C1052). DNA content was analyzed by flow cytometry, and cell fractions in G0/G1, S, and G2/M phases were determined.

HR-pathway canonical marker analysis: To further corroborate the HR-pathway involvement suggested by γH2AX/RAD51 immunoblotting, mRNA levels of the canonical BRCA1-PALB2-BRCA2-RAD51 HR mediator axis were assessed by qRT-PCR, and BRCA1, PALB2, and BRCA2 protein levels were examined by Western blot in si-NC- and si-SMC1B-transfected PC-3 and LNCaP cells. Primer sequences and antibody information are listed in Supplementary Table 1.

AR blockade experiment: To interrogate whether SMC1B-dependent perturbation of HR medi-

ators is modulated by androgen receptor (AR) signaling, AR-positive LNCaP cells were treated with 10 μM enzalutamide (ENZ; Selleckchem, S1250) or an equivalent volume of 0.1% DMSO (vehicle) for 48 h, in combination with si-NC or si-SMC1B transfection, generating four groups: si-NC+DMSO, si-SMC1B+DMSO, si-NC+ENZ, and si-SMC1B+ENZ. Pharmacological blockade of AR activity was confirmed by Western blot of AR and PSA, and by qRT-PCR of AR and KLK3. Downstream HR-related readouts included BRCA1, RAD51, and γH2AX (Western blot) as well as BRCA1 and RAD51 mRNA (qRT-PCR). The ENZ concentration and vehicle protocol follow previous research [20].

Statistical analysis

All data are presented as mean ± SD unless otherwise indicated. Normality was assessed by the Shapiro-Wilk test and homogeneity of variance by Levene's test. When both assumptions were satisfied, two-group comparisons used independent-sample Student's t-test or paired t-test. Multiple-group comparisons used one-way ANOVA with Tukey's post hoc test; time-course CCK-8 data were analysed by two-way repeated-measures ANOVA with Bonferroni correction. When parametric assumptions were violated, non-parametric alternatives were applied. Bioinformatic high-throughput comparisons (differential expression, WGCNA module-trait correlation, GSEA, and single-cell enrichment scoring) were corrected for multiple testing using the Benjamini-Hochberg FDR. All cellular experiments were performed as three independent biological replicates, each containing three technical replicates; replicate structure is specified in figure legends. Statistical analyses used R v4.2.2 and GraphPad Prism v10.0. P or adj.P < 0.05 was considered statistically significant.

Results

MR analysis of SMC1B and PRAD

MR analysis demonstrated a robust causal relationship between SMC1B and PRAD risk (**Figure 1A**). A total of 10 independent cis-eQTL SNPs were identified as instrumental variables. Individual F-statistics for these instruments ranged from 33.94 to 344.94 (mean F = 80.33), well exceeding the empirical threshold of 10 and ruling out weak instrument bias. The scatter plot showed consistent positive slopes across multiple MR methods (MR-Egger, weighted median, inverse variance weighted, simple mode, and weighted mode) with intercepts near 0 (**Figure 1B**), while the funnel plot indicated that individual SNP effect estimates aligned well with the IVW estimate (**Figure 1C**). Sensitivity analyses confirmed the robustness of these findings: heterogeneity test (P > 0.05, Supplementary Table 2) and horizontal pleiotropy test (P > 0.05, Supplementary Table 3) revealed no significant heterogeneity or pleiotropy; Steiger directionality test (P < 0.05, Supplementary Table 4) strongly supported the correct causal direction from SMC1B expression to PRAD risk; and leave-one-out analysis demonstrated that causal effect estimates remained stable when excluding any single SNP sequentially (**Figure 1D**), indicating that the results did not depend on any individual SNP and further confirming the reliability of the causal relationship between SMC1B and PRAD.

SMC1B expression and clinical prognostic value analysis

To evaluate the clinical significance of SMC1B in PRAD, expression analysis revealed significantly elevated SMC1B levels in PRAD tissues compared to normal controls (P < 0.001, **Figure 2A**), suggesting its involvement in PRAD pathogenesis. Univariate Cox regression analysis identified SMC1B expression and T stage as significantly associated with overall survival (**Figure 2B**), which were subsequently confirmed as independent prognostic factors in multivariate analysis (**Figure 2C**). Notably, SMC1B expression showed no significant differences across T stages (**Figure 2D**), indicating its prognostic value may be independent of local tumor invasion. Kaplan-Meier survival analysis demonstrated significantly shorter overall survival in the SMC1B high expression group (P = 0.00921, HR = 1.75, 95% CI: 1.15-2.66, **Figure 2E**), while time-dependent ROC curves showed moderate prognostic value, with AUCs of 0.64 (95% CI: 0.53-0.75), 0.60 (95% CI: 0.53-0.67), and 0.57 (95% CI: 0.48-0.65) for 1-, 3-, and 5-year overall survival, respectively (**Figure 2F**). The gradual decline of AUC over time, together with 95% confidence intervals that approach 0.5 at later time points, indicates that the long-term discrimina-

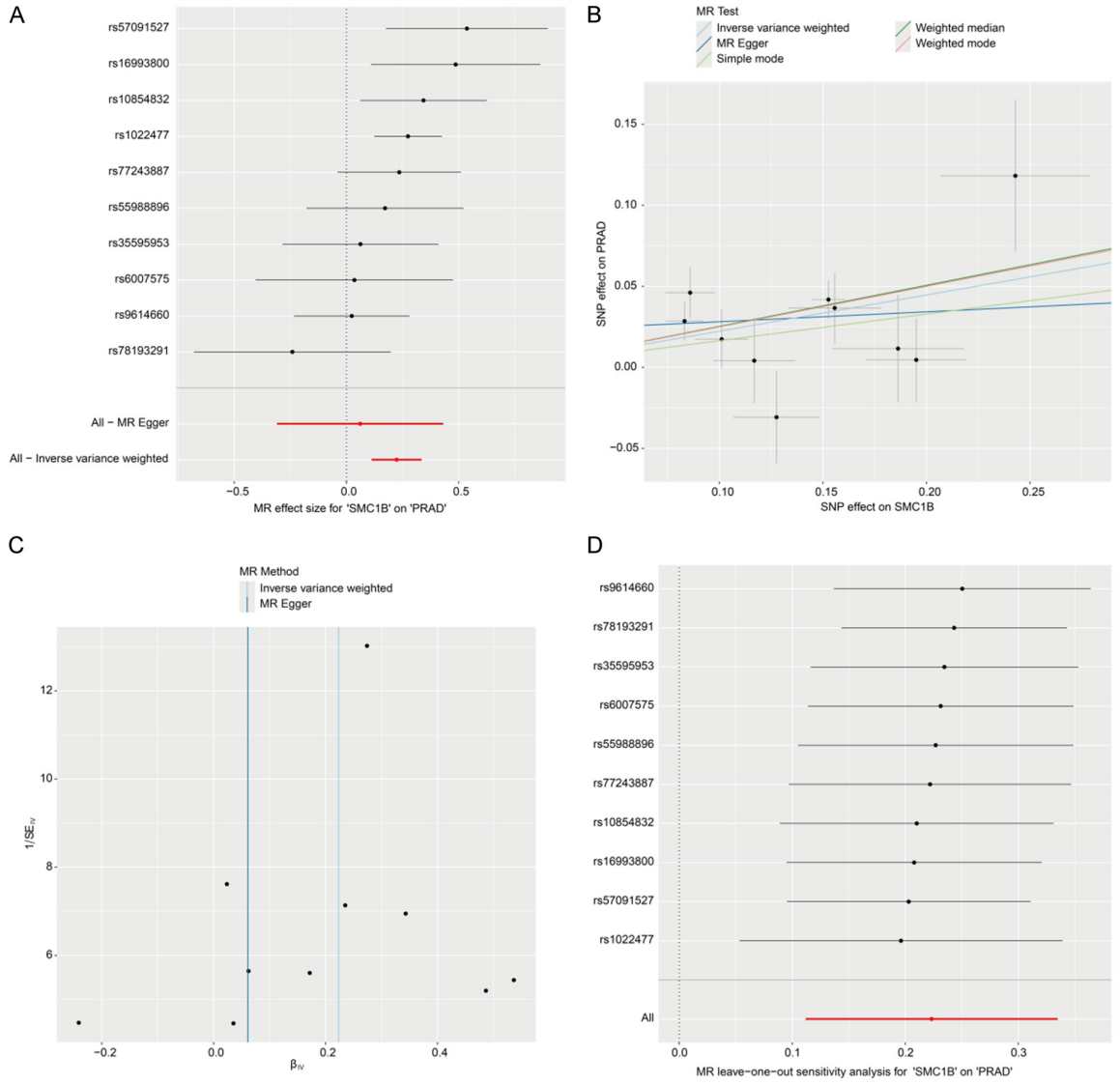

Figure 1. Mendelian randomization analysis results of SMC1B and ProstateCancer (PRAD) risk. A. Forest plot of SMC1B gene expression quantitative trait loci (eQTL). B. Scatter plot of SMC1B gene. C. Funnel plot of SMC1B gene. D. Leave-one-out analysis of SMC1B gene. Causal estimates were derived using the inverse-variance weighted method with MR-Egger, weighted median, simple mode, and weighted mode as sensitivity analyses.

tory stability of SMC1B as a single prognostic marker is limited. To explore whether combining SMC1B with routine clinicopathological variables could compensate for this limitation, a prognostic nomogram integrating SMC1B expression, age, and T stage was constructed (Supplementary Figure 1A), with calibration curves demonstrating acceptable consistency between predicted and observed survival (Supplementary Figure 1B), and decision curve analysis showing modest net benefit relative to single-parameter models (Supplementary Figure 1C). These exploratory results suggest that SMC1B may serve as a complementary, rather than stand-alone, molecular indicator for prognostic evaluation in PRAD.

Identification of SMC1B co-expressed genes

Through differential expression analysis, this study detected a large number of significantly altered genes in PRAD tissues. The volcano plot clearly displayed the overall distribution pattern of gene expression changes, where red dots represent genes significantly upregulated in tumors, blue dots represent significantly

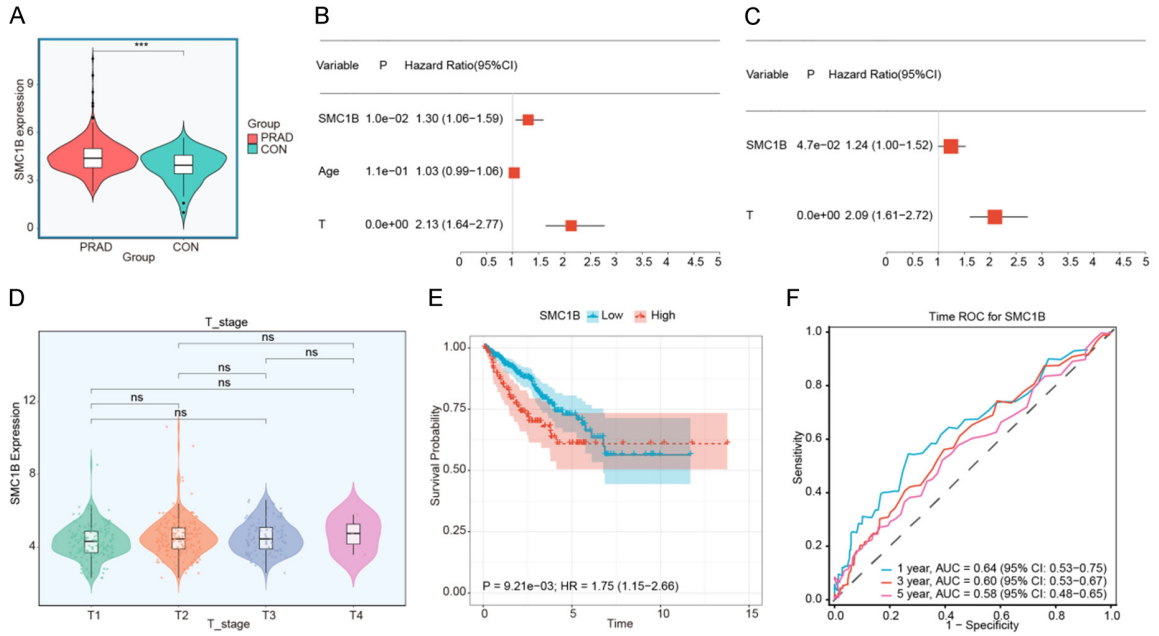

Figure 2. Expression characteristics and clinical prognostic value of SMC1B in PRAD. A. Comparison of SMC1B expression levels in PRAD and normal control (CON) tissues. B. Univariate Cox regression analysis forest plot. C. Multivariate Cox regression analysis forest plot. D. Distribution of SMC1B expression in different T stages. E. Kaplan-Meier survival curves based on SMC1B expression grouping. F. Time-dependent ROC curves. ns, not significant; *P < 0.05, **P < 0.01, ***P < 0.001. Statistical significance: A. Wilcoxon rank-sum test; B, C. Cox proportional hazards regression; D. Kruskal-Wallis test; E. Log-rank test.

downregulated genes, and hundreds of genes reached the preset differential expression threshold (**Figure 3A**). The top 20 genes with the most significant expression changes were displayed through a heatmap (**Figure 3B**).

WGCNA analysis successfully constructed a gene co-expression network related to PRAD. During network construction, the scale-free topology fit index reached the ideal level of 0.8 when the soft-thresholding power was 5, ensuring the biological relevance of the network (**Figure 3C**). At this time, the mean connectivity was maintained within a reasonable range, ensuring the stability and interpretability of the network (**Figure 3D**). Based on optimized network parameters, seven functional modules were identified, with each module containing varying numbers of co-expressed genes, reflecting different molecular regulatory programs during the occurrence and development of PRAD (**Figure 3E**). Module-trait association analysis revealed key functional modules closely related to PRAD. Among them, magenta, green, midnightblue, purple, salmon, black, and turquoise were significantly correlated with clinical phenotypes (**Figure 3F**). A total of 1970 co-expressed genes were obtained from these modules as candidate genes.

Functional enrichment analysis of candidate genes

To elucidate the biological functions and signaling cascades associated with SMC1B, KEGG and GO (BP, CC, MF) enrichment analyses were performed on SMC1B together with its 1,970 co-expressed candidate genes (Supplementary Figure 2A). KEGG pathway analysis prominently highlighted genomic-integrity and therapeutic-response pathways, including the Fanconi anemia pathway, Homologous recombination, and Platinum drug resistance, together with oncogenic cascades such as FoxO and TGF-β signaling. GO terms converged on chromosome behavior and DNA metabolism (BP: DNA recombination, replication fork processing, maintenance of DNA replication fidelity; CC: nuclear chromosome, replication fork, heterochromatin; MF: ATP-dependent activity acting on DNA, DNA helicase activity).

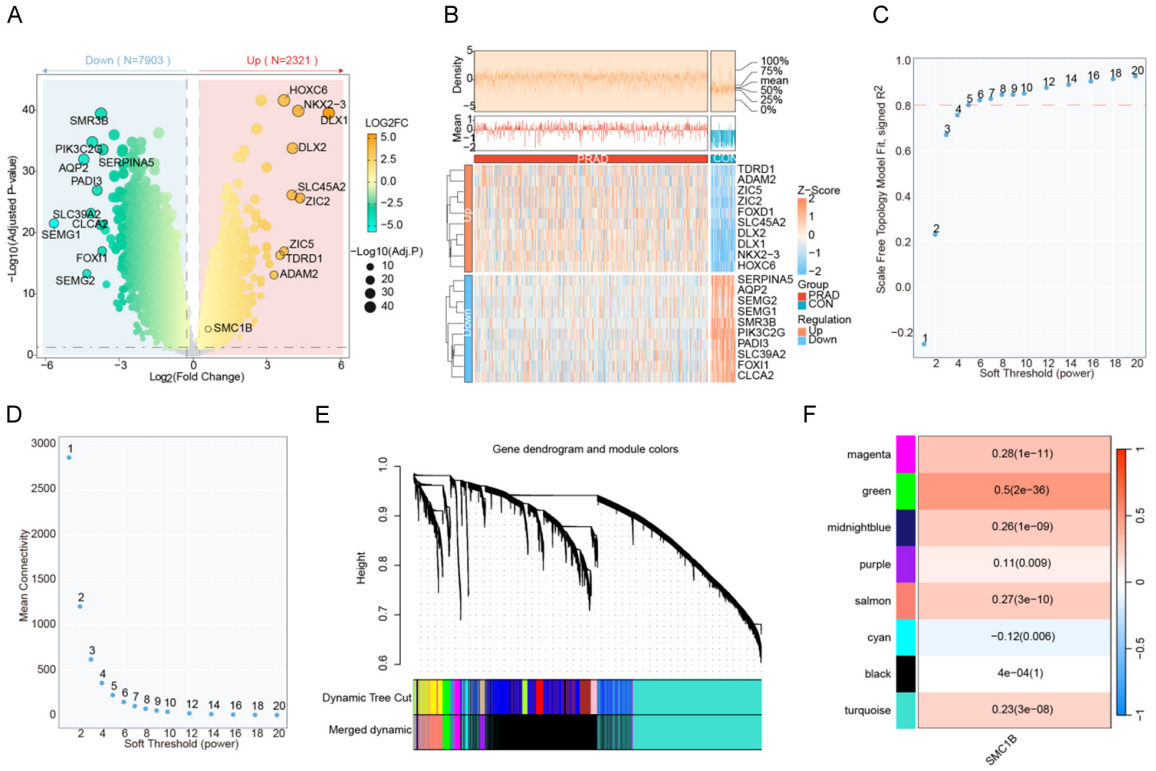

Figure 3. Differential gene screening and weighted gene co-expression network analysis. A. Volcano plot of differentially expressed genes. B. Heatmap displaying the top 20 genes with the most significant expression changes. C. Soft-thresholding power selection: relationship between scale-free topology fit index and soft-thresholding power. D. Relationship between mean connectivity and soft-thresholding power. E. Gene clustering dendrogram and module identification, with different colors representing different modules. F. Module-trait correlation heatmap, values represent correlation coefficients, with *P* values in parentheses.

Single-gene GSEA further validated these pathways between SMC1B-high and -low groups (Supplementary Figure 2B): the Fanconi anemia pathway, Homologous recombination, Cell cycle, and ATP-dependent chromatin remodeling were significantly up-regulated in SMC1B-high tumors (NES > 0, adj. P < 0.05), whereas the Proteasome and branched-chain amino-acid degradation pathways were down-regulated (NES < 0, adj. P < 0.05).

Chord-network mapping of the two most enriched DNA-repair pathways identified 21 Fanconi-anemia genes (e.g., FANCA, FANCM, UBE2T, ERCC4) and 12 homologous-recombination genes (e.g., ATM, RAD50, RAD54L, POLD2), with five shared genomic guardians - BLM, EME1, PALB2, RAD51, and RPA1 - cross-linking both pathways (Supplementary Figure 2C). This architecture supports the notion that SMC1B operates within an integrated DNA-repair machinery to maintain genome stability in PRAD cells.

SMC1B functional gene set scoring and intercellular communication network analysis based on single-cell transcriptomics

Unsupervised clustering of the GSE176031 dataset partitioned cells into eight canonical lineages: epithelial, basal, endothelial, fibroblast, macrophage, smooth muscle, mast, and T cells (Supplementary Figure 3A, 3B). Compositional profiling revealed hallmark microenvironmental remodeling in PRAD: the epithelial fraction expanded from 49.6% (CON) to 57.5% (PRAD), while basal cells decreased from 20.0% to 18.3% and T cells sharply declined from 8.4% to 3.4% (Supplementary Figure 3C), reflecting malignant clonal outgrowth and local immunosuppression.

Intersecting single-cell DEGs (n = 456) with WGCNA hub genes (n = 1,970) yielded a 24-gene SMC1B functional set (Supplementary Figure 3D; full annotations in Supplementary Table 5) that includes the central HR recombi-

nase RAD51, directly linking the single-cell signature to our bulk HR/Fanconi enrichment cascades.

We next scored this 24-gene set using three complementary algorithms (AUCell, PercentageFeatureSet, and ssGSEA). All three algorithms consistently showed that the SMC1B score was markedly elevated in PRAD versus CON tissues ($P < 0.0001$; **Figure 4A**) and was selectively enriched in epithelial cells relative to stromal and immune compartments (**Figure 4B-D**). Lineage-stratified comparison confirmed that malignant epithelial cells displayed the most pronounced upregulation of SMC1B score over normal epithelial cells ($P < 0.0001$; **Figure 4E-G**), identifying malignant epithelial cells as the primary cellular compartment executing SMC1B-mediated oncogenic functions.

CellChat analysis further decoded how malignant epithelial cells orchestrate microenvironmental crosstalk (**Figure 5A**, **5B**). Epithelial cells exhibited the highest interaction count with basal cells and the strongest communication intensity with endothelial and T cells. Key ligand-receptor axes included HBEGF-EGFR, VEGFA-VEGFR1/2, APP-CD74, JAG1-NOTCH2, and COL1A1-ITGA1-ITGB1. The complete set of significant L-R pairs is shown as a heatmap in **Figure 5B**.

SMC1B expression is elevated in PRAD tissues and is effectively silenced by siRNA

IHC staining of paired PRAD and CON tissue specimens qualitatively confirmed epithelial SMC1B expression and showed visibly stronger immunoreactivity in tumor sections than in paired controls (**Figure 6A**). Western blot of three paired specimens consistently showed higher SMC1B protein in PRAD tissues (**Figure 6B**, **6E**). In agreement, qRT-PCR detected an increase in SMC1B mRNA in PRAD relative to CON ($P < 0.001$; **Figure 6F**). Together, these data indicate that SMC1B is up-regulated in PRAD at both transcriptional and translational levels.

To enable loss-of-function studies, PC-3 and LNCaP cells were transfected with SMC1B-targeting siRNA (si-SMC1B) or non-targeting control siRNA (si-NC). qRT-PCR confirmed efficient knockdown of SMC1B mRNA in both PC-3 (**Figure 6G**) and LNCaP (**Figure 6H**) cells ($P < 0.001$). Western blot (**Figure 6C**, **6D**, **6I**, **6J**) demonstrated a parallel reduction in SMC1B protein in PC-3 and LNCaP cells ($P < 0.001$), establishing adequate knockdown efficiency for downstream functional analyses.

SMC1B silencing is associated with altered DNA damage repair marker expression and reduced cell proliferation

Functional enrichment analyses revealed that SMC1B and co-expressed marker genes were significantly enriched in homologous recombination (HR), the Fanconi anemia pathway, and DNA replication fidelity maintenance, with single-gene GSEA further confirming that both HR and the Fanconi anemia pathway were significantly upregulated in the SMC1B-high expression group ($NES > 1$, $P < 0.05$; Supplementary Figure 2). These bioinformatic findings prompted us to examine whether SMC1B silencing perturbed the expression of key molecular markers associated with these pathways. Western blot showed that, compared with si-NC controls, SMC1B knockdown was associated with elevated γH2AX levels and reduced RAD51 expression in both PC-3 and LNCaP cells ($P < 0.001$; **Figure 7A**, **7B**). To interrogate whether SMC1B knockdown perturbs the broader HR mediator axis rather than the terminal RAD51 effector alone, we next evaluated the canonical BRCA1-PALB2-BRCA2 mediator cascade. Western blot analysis revealed concomitant reductions in BRCA1, PALB2, and BRCA2 protein levels in si-SMC1B cells relative to si-NC controls in both PC-3 (**Figure 7C**) and LNCaP (**Figure 7D**) cells (all $P < 0.001$). Consistent down-regulation of BRCA1, PALB2, BRCA2, and RAD51 was also observed at the mRNA level in both cell lines (Supplementary Figure 4A-H). Because BRCA1, PALB2, and BRCA2 together scaffold RAD51 loading at resected DSB ends [21], the convergent down-regulation of all four HR mediators supports the interpretation that SMC1B silencing is associated with a system-level perturbation of HR competence rather than an isolated effect on a single effector.

SMC1B silencing is associated with reduced cell migration and invasion in vitro

We next evaluated the cellular consequences of SMC1B silencing on proliferation and clonogenic potential. CCK-8 time-course assays

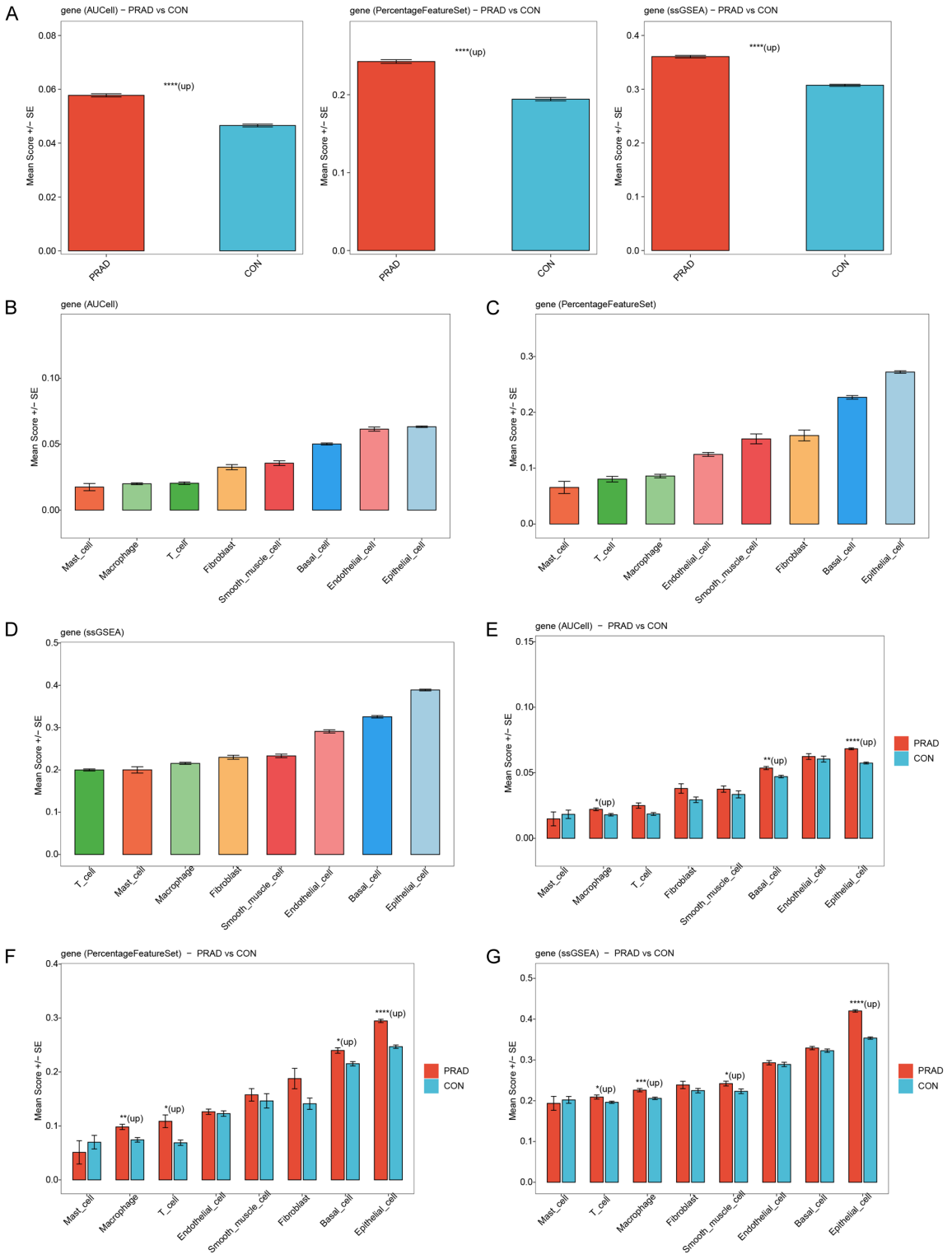

Figure 4. Multi-algorithmic single-cell scoring of the SMC1B 24-gene functional signature across prostate tissue lineages. (A) Comparison of SMC1B functional gene set scores between PRAD and CON tissues evaluated by three independent algorithms: AUCell (left), PercentageFeatureSet (middle), and ssGSEA (right). Data represent mean ± SE; ****P < 0.0001. (B-D) Cell-type-specific distribution of SMC1B functional scores across eight annotated cell lineages in GSE176031 quantified by AUCell (B), PercentageFeatureSet (C), and ssGSEA (D). Bars are ordered hierarchically, showing predominant activity in epithelial cells. (E-G) Grouped comparison of SMC1B functional scores

between PRAD and CON across individual cell lineages evaluated by AUCell (E), PercentageFeatureSet (F), and ssGSEA (G). Epithelial cells display the most significant elevation in PRAD. Data represent mean ± SE; *adj.P < 0.05, **adj.P < 0.01, ***adj.P < 0.001, ****adj.P < 0.0001; Wilcoxon rank-sum test with Benjamini-Hochberg correction.

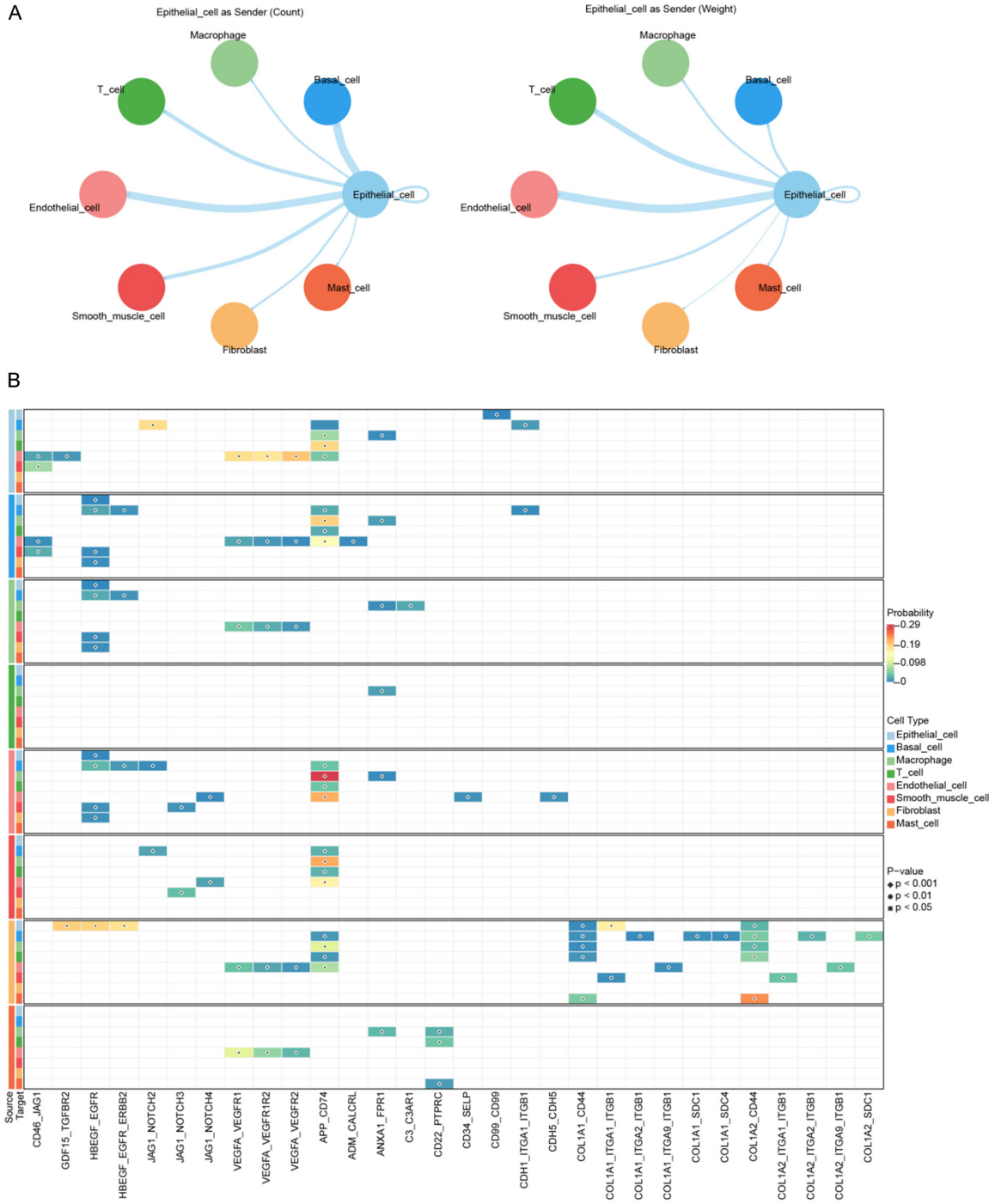

Figure 5. Intercellular communication networks and ligand-receptor cross-talk centered on malignant epithelial cells. A. Chordal communication network inferred by CellChat displaying interaction number (left, Count) and interaction strength (right, Weight) with epithelial cells designated as the primary signaling source across microenvironmental cell types. B. Heatmap resolving significant ligand-receptor pairs across cell types.

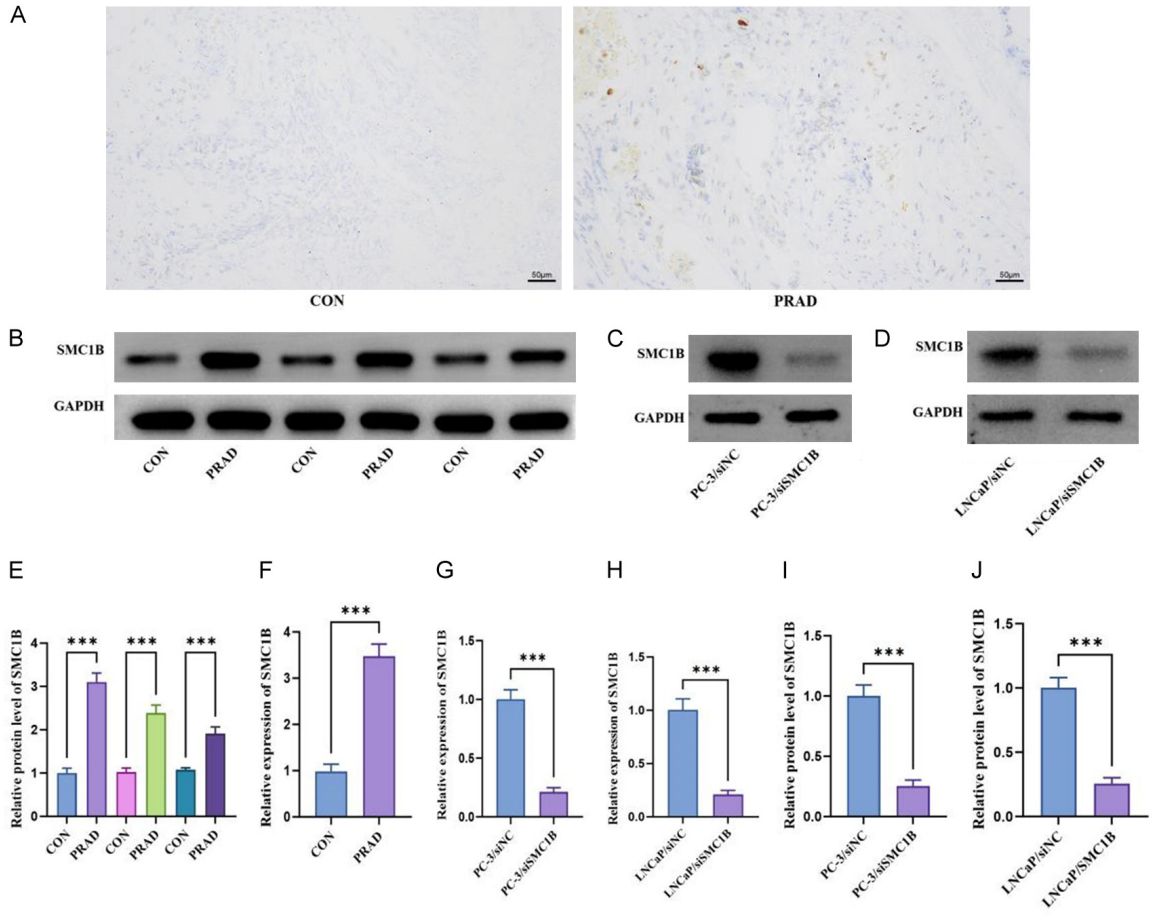

Figure 6. SMC1B expression in PRAD tissues and siRNA-mediated knockdown efficiency in PC-3 and LNCaP cells. (A) Representative immunohistochemical staining of SMC1B in paired CON and PRAD tissue sections, shown as qualitative confirmation of epithelial SMC1B localisation and of the direction of up-regulation in tumor tissue (×400 magnification; scale bar, 50 μm). (B) Representative Western blot of SMC1B and GAPDH in three paired CON and PRAD tissue specimens. (C, D) Representative Western blot of SMC1B and GAPDH in PC-3 (C) and LNCaP (D) cells. (E) Densitometric quantification of SMC1B protein levels normalized to GAPDH in the three paired tissue specimens shown in (B). (F) qRT-PCR quantification of SMC1B mRNA levels in paired CON and PRAD tissues (n = 3 pairs). (G, H) qRT-PCR quantification of SMC1B mRNA levels in PC-3 (G) and LNCaP (H) cells. (I, J) Densitometric quantification of SMC1B protein levels normalized to GAPDH in PC-3 (I) and LNCaP (J) cells. Data are presented as mean ± SD (n = 3 biological replicates); ***P < 0.001 by paired two-tailed t-test (E, F) or unpaired two-tailed t-test (G-J).

showed significantly reduced cell viability in si-SMC1B groups relative to si-NC controls at 48 and 72 h in both PC-3 and LNCaP cells ($P < 0.001$; **Figure 8A**). Colony formation assays showed markedly fewer and smaller colonies in si-SMC1B groups than in si-NC controls in both cell lines (**Figure 8B-D**).

To assess motility and invasiveness, Transwell invasion and wound-healing assays were performed. Transwell images revealed a visibly lower number of invaded si-SMC1B cells than si-NC controls in both cell lines (**Figure 8E-G**). Consistently, wound-healing assays showed that scratch closure at 24 h was markedly reduced in si-SMC1B groups relative to si-NC controls in PC-3 and LNCaP (**Figure 8H-J**). Collectively, these observations indicate that SMC1B expression is associated with the proliferative, clonogenic, migratory, and invasive potential of PRAD cells *in vitro*.

SMC1B silencing is associated with cell-cycle redistribution and increased apoptosis

Flow-cytometric analysis showed that SMC1B knockdown was associated with a significant increase in the G0/G1 fraction and a concurrent reduction in the S and G2/M fractions compared with si-NC controls in both PC-3 and

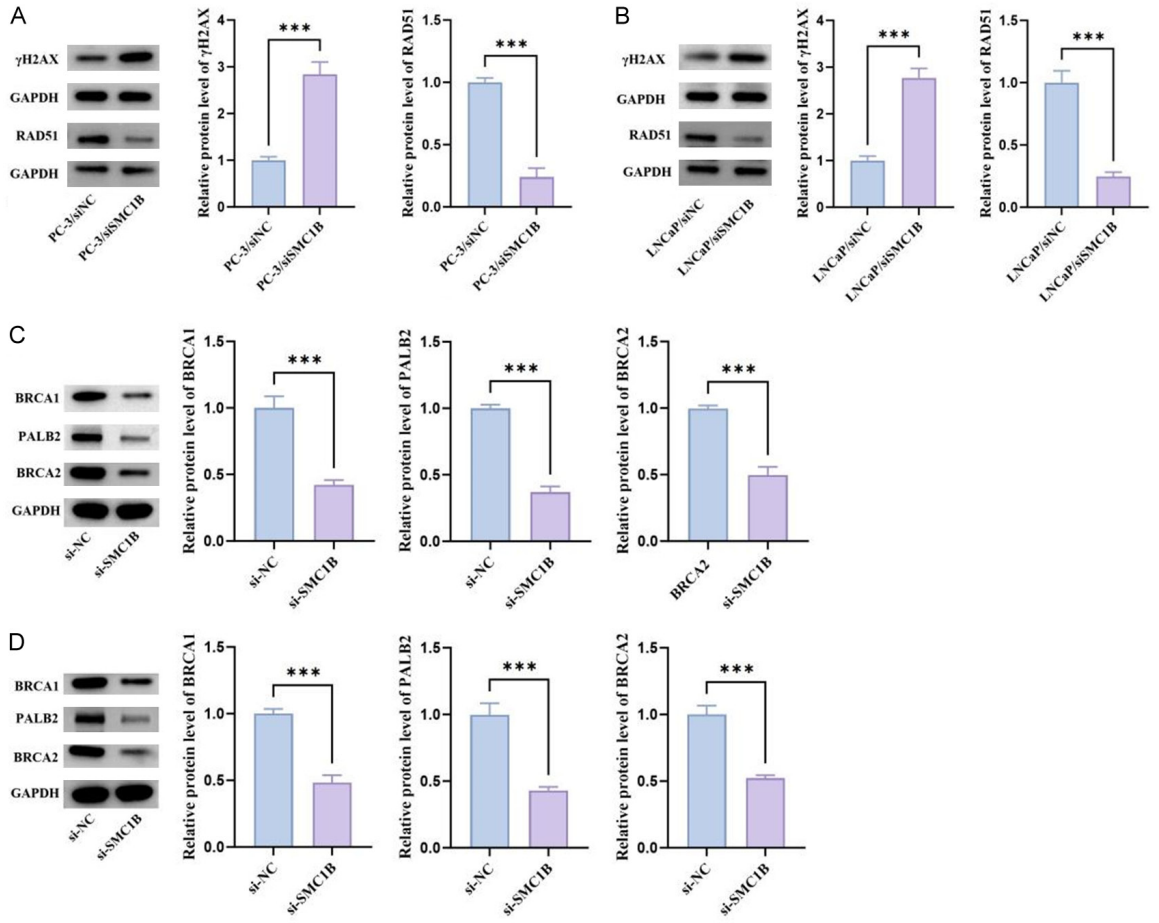

Figure 7. SMC1B knockdown coordinately down-regulates the BRCA1-PALB2-BRCA2-RAD51 homologous recombination mediator axis in PC-3 and LNCaP cells. (A, B) Representative Western blot of γH2AX, RAD51, and GAPDH, together with densitometric quantification of γH2AX and RAD51 protein levels normalized to GAPDH, in si-NC- and si-SMC1B-transfected PC-3 (A) and LNCaP (B) cells. (C, D) Representative Western blot of BRCA1, PALB2, BRCA2, and GAPDH, together with densitometric quantification of BRCA1, PALB2, and BRCA2 protein levels normalized to GAPDH, in si-NC- and si-SMC1B-transfected PC-3 (C) and LNCaP (D) cells. Data are presented as mean ± SD (n = 3 biological replicates); ***P < 0.001 by unpaired two-tailed t-test.

LNCaP cells (P < 0.05 to P < 0.001; **Figure 9A**, **9B**, **9E**, **9F**). Annexin V-FITC/PI staining showed that the proportion of apoptotic cells (early and late combined) was significantly higher in si-SMC1B groups than in si-NC controls in both cell lines (P < 0.001; **Figure 9C**, **9D**, **9G**, **9H**). These findings suggest that SMC1B silencing may influence cell-cycle progression and apoptotic responses in PRAD cells, though the precise regulatory mechanisms remain to be elucidated.

AR signalling partially modulates SMC1B-dependent HR perturbation

At the protein level, AR expression was unchanged across groups (**Figure 10A**, **10B**), whereas its canonical target PSA was substantially suppressed by ENZ in both si-NC and si-SMC1B contexts (**Figure 10A**, **10C**; P < 0.001). Consistently, mRNA levels of AR were comparable across groups (**Figure 10G**), while KLK3 (encoding PSA) was markedly down-regulated by ENZ (**Figure 10H**; P < 0.001), confirming effective pharmacological blockade of AR transcriptional activity.

At the HR-mediator level, SMC1B knockdown alone reduced BRCA1 and RAD51 at both protein (**Figure 10A**, **10D**, **10E**; P < 0.001) and mRNA (**Figure 10I**, **10J**; P < 0.001) levels, while concomitantly elevating γH2AX (**Figure 10A**, **10F**; P < 0.001). Notably, AR-negative PC-3 cells exhibited HR-mediator reductions of com-

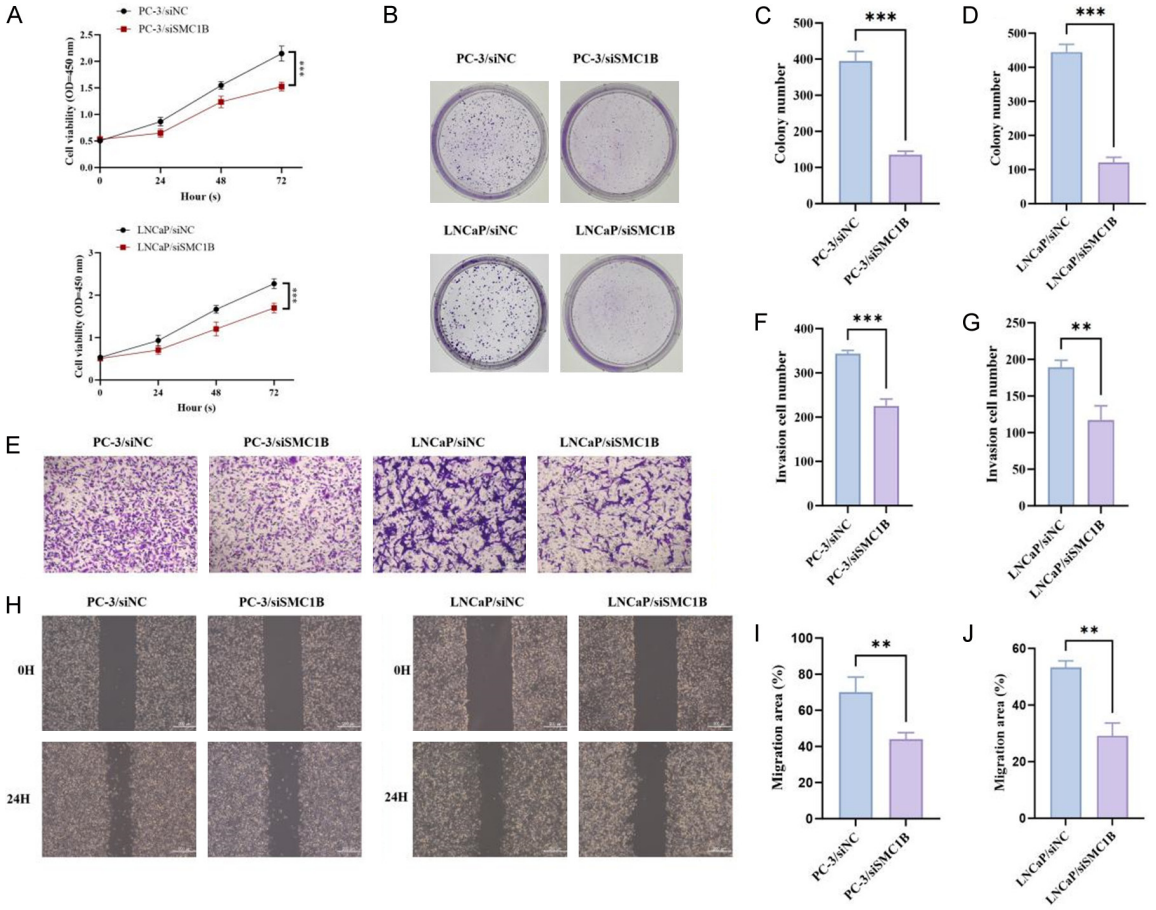

Figure 8. SMC1B knockdown suppresses proliferation, clonogenicity, migration, and invasion of PC-3 and LNCaP cells. (A) CCK-8 cell viability measured at 0, 24, 48, and 72 h in si-NC- and si-SMC1B-transfected PC-3 (upper) and LNCaP (lower) cells. (B) Representative images of colony formation assays in si-NC- and si-SMC1B-transfected PC-3 (upper) and LNCaP (lower) cells. (C, D) Quantification of colony numbers in PC-3 (C) and LNCaP (D) cells. (E) Representative images of crystal violet-stained invaded cells from Transwell assays in si-NC- and si-SMC1B-transfected PC-3 (left two panels) and LNCaP (right two panels) cells (scale bar, 100 μm). (F, G) Quantification of invaded cell numbers per field in PC-3 (F) and LNCaP (G) cells. (H) Representative wound-healing images captured at 0 h and 24 h in si-NC- and si-SMC1B-transfected PC-3 (left) and LNCaP (right) cells (scale bar, 200 μm). (I, J) Quantification of scratch closure (migration area %) at 24 h in PC-3 (I) and LNCaP (J) cells. Data are presented as mean ± SD (n = 3 biological replicates); **P < 0.01, ***P < 0.001 by unpaired two-tailed t-test (C, D, F, G, I, J) or by two-way repeated-measures ANOVA with Bonferroni correction (A).

parable magnitude to AR-positive LNCaP cells after SMC1B knockdown (**Figure 7A-D** and Supplementary Figure 4A-H), further supporting an AR-independent function of SMC1B in sustaining the HR mediator axis in PRAD cells.

Discussion

In this study, we provide an integrated causal, transcriptomic, and experimental dissection of SMC1B in PRAD. Mendelian randomization established a directional causal link between elevated SMC1B and PRAD risk; bulk and single-cell transcriptomic analyses converged on homologous-recombination-related programs and pinpointed malignant epithelial cells as the principal site of SMC1B activity; and siRNA-mediated SMC1B knockdown in PC-3 and LNCaP cells produced a coherent oncogenic-loss phenotype - elevated γH2AX, reduced RAD51, decreased proliferation, impaired migration/invasion, G0/G1 arrest, and increased apoptosis. This convergence of genetic, transcriptomic, and functional evidence places SMC1B at the intersection of DNA damage repair and PRAD progression, and supports further investigation of SMC1B as a candidate prognostic biomarker in PRAD.

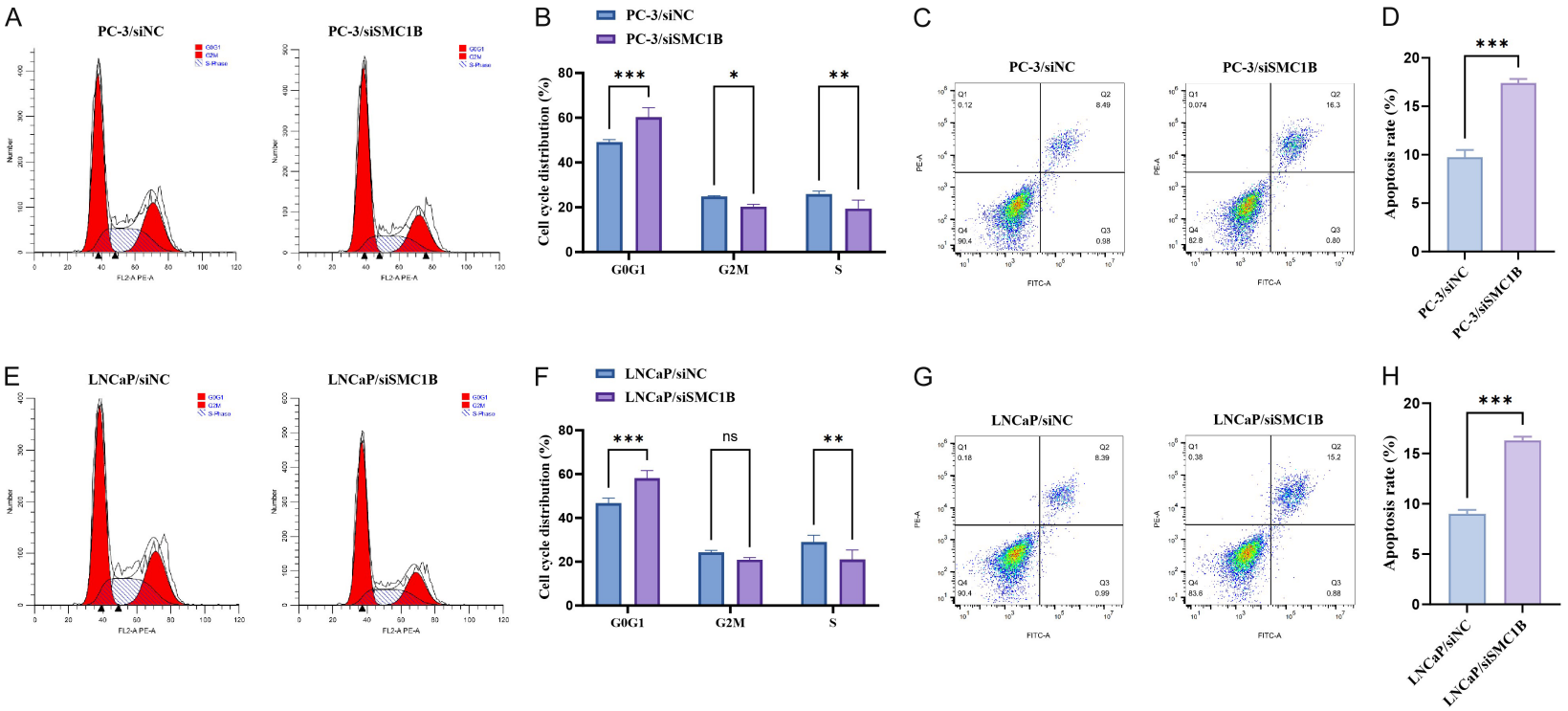

Figure 9. Effects of SMC1B knockdown on cell-cycle distribution and apoptosis in PC-3 and LNCaP cells. (A, E) Representative PI-stained flow-cytometric histograms of cell-cycle profiles in PC-3 (A) and LNCaP (E) cells. (B, F) Quantification of cell fractions in G0/G1, S, and G2/M phases in PC-3 (B) and LNCaP (F) cells. (C, G) Representative Annexin V-FITC/PI dot plots of PC-3 (C) and LNCaP (G) cells; Q2 and Q3 indicate late- and early-apoptotic populations, respectively. (D, H) Quantification of total apoptosis rates in PC-3 (D) and LNCaP (H) cells. Data are presented as mean ± SD (n = 3 biological replicates); ns, not significant; *P < 0.05, **P < 0.01, ***P < 0.001 by unpaired two-tailed Student's t-test. Normality of distributions was confirmed by the Shapiro-Wilk test prior to parametric testing.

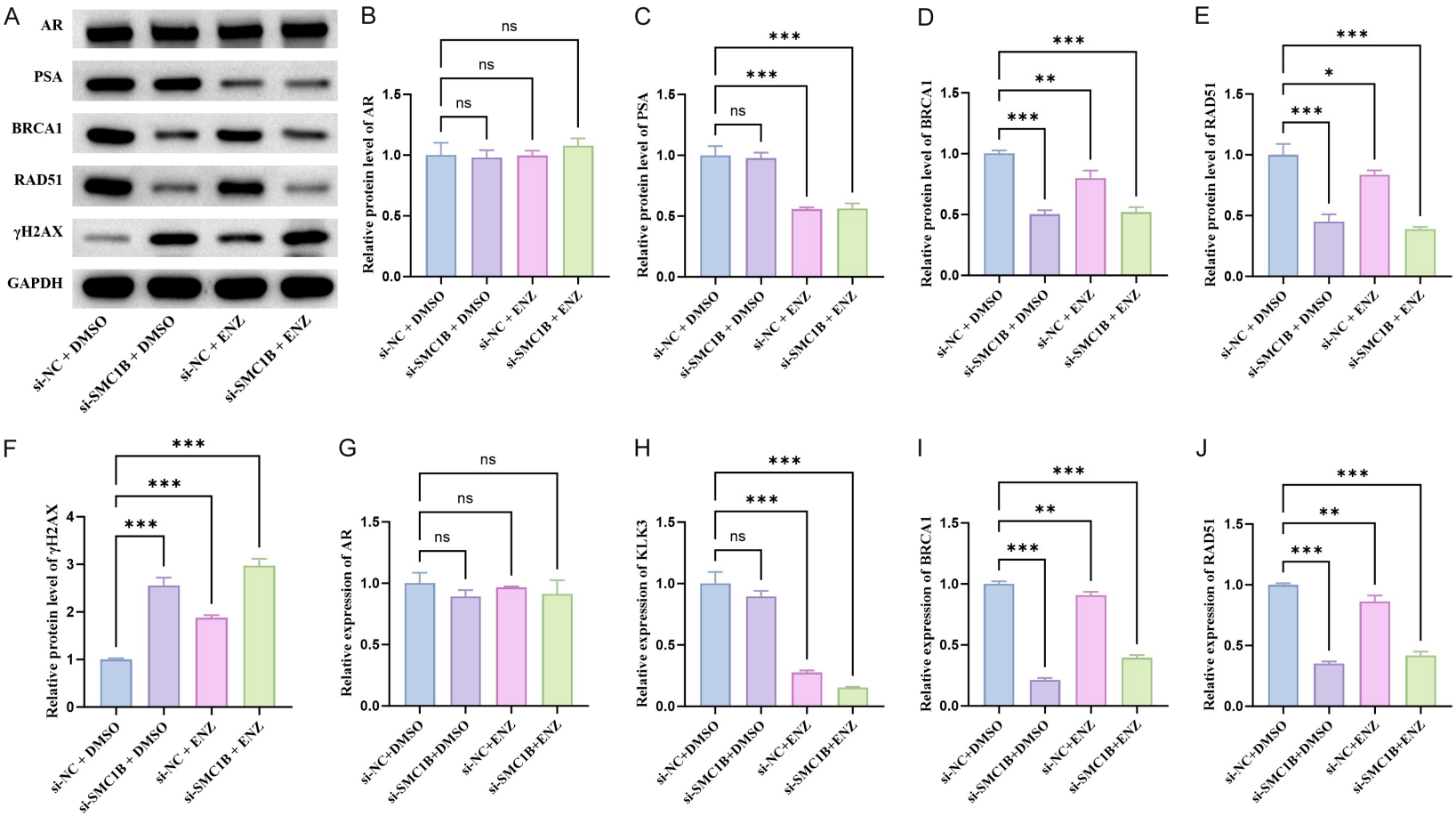

Figure 10. SMC1B regulates HR mediators independently of AR signaling in LNCaP cells. (A) Representative Western blot of AR, PSA, BRCA1, RAD51, γH2AX, and GAPDH across the four treatment groups. (B-F) Densitometric quantification of AR (B), PSA (C), BRCA1 (D), RAD51 (E), and γH2AX (F) protein levels normalized to GAPDH. (G-J) qRT-PCR quantification of AR (G), KLK3 (H), BRCA1 (I), and RAD51 (J) mRNA levels. Data are presented as mean ± SD (n = 3 biological replicates); ns, not significant; *P < 0.05, **P < 0.01, ***P < 0.001 by two-way ANOVA with Tukey's post-hoc test. Statistical results are referenced to the si-NC+DMSO group unless otherwise indicated.

MR Analysis showed a significant causal association between elevated SMC1B expression and an increased risk of PRAD ($P < 0.05$). In recent years, MR Methods have been widely used in the study of tumor etiology [22]. As a member of the structural maintenance chromosomal protein family, SMC1B has gradually attracted attention in tumorigenesis [23]. Studies on hepatocellular carcinoma have found that high expression of SMC family protein RAD21 (a member of the cohesion complex) is associated with poor prognosis of patients, suggesting the importance of the cohesion complex in tumor progression [24]. This study extends these mechanistic observations to the human disease setting for the first time.

A mechanistically significant finding of this study is that silencing of SMC1B simultaneously increased levels of γH2AX (a recognised marker of unrepaired double-strand breaks, DSBs) [25], whilst simultaneously reducing levels of RAD51 (the core recombinase of homologous recombination (HR) and a functional marker of HR competence) [26]. SMC1B knockdown led to a concordant perturbation of the BRCA1-PALB2-BRCA2-RAD51 HR mediator axis, with concurrent γH2AX accumulation. While these converging biomarker changes are consistent with impaired HR competence - a state functionally analogous to BRCAness - we emphasise that direct quantitative evidence of DSB repair kinetics (e.g., post-IR/etoposide/HU RAD51 foci formation and neutral comet assays) was not performed in the present study due to equipment constraints. Our evidence should therefore be interpreted as mechanistically suggestive rather than definitive. Clinically, patients with metastatic PRAD harbour defects in HR-related genes (such as BRCA2, ATM and CHEK2), which confer sensitivity to PARP inhibitors and platinum-based regimens [27, 28].

Consistent with impaired genomic integrity, silencing of SMC1B inhibits cell proliferation, induces G0/G1 arrest, and increases apoptosis. These phenotypes are similar to those previously reported for the related cohesin subunit SMC1A in lung adenocarcinoma cells, where its loss similarly resulted in G1/S phase arrest, reduced clonogenicity and increased apoptosis [29]. Mechanistically, SMC1B is essential for the spatial organisation of the replication factory and tolerance to replication-related damage. Loss of cohesin function during S phase leads to replication fork stalling and unrepaired DSBs, thereby triggering checkpoint-mediated G0/G1 arrest; when damage cannot be repaired, it also induces programmed cell death, providing a mechanistic basis for the proliferation and survival phenotypes observed following SMC1B knockdown.

Silencing of SMC1B also impairs the migratory and invasive capabilities of PRAD cells. Although the regulation of motility is not a traditional function of cohesins, unresolved replicative stress activates the ATR/ATM signalling pathway, which influences metastatic capacity by transcriptionally remodelling the cytoskeleton and processes associated with epithelial-mesenchymal transition. In our single-cell analysis, SMC1B functional enrichment was predominantly concentrated in malignant epithelial cells - the region where an epithelial-mesenchymal-like transcriptional state emerges during PRAD progression [19] - suggesting that SMC1B may indirectly maintain the invasive phenotype by preserving the genomic and transcriptional integrity of this malignant cellular compartment. Notably, the oncogenic-loss phenotypes described above - impaired proliferation, G0/G1 arrest, increased apoptosis, and reduced migration and invasion - were observed consistently across both PC-3 (AR-negative, castration-resistant) and LNCaP (AR-positive, androgen-sensitive) cells, two models representing biologically distinct PRAD subtypes. This cross-subtype concordance suggests that SMC1B-dependent maintenance of HR-mediated genome stability may constitute a core survival mechanism that operates independently of androgen receptor signaling status, thereby broadening the potential clinical relevance of SMC1B as a potential biomarker across the heterogeneous spectrum of PRAD.

Beyond core DNA repair mechanisms, our functional enrichment analyses also highlighted the Platinum drug resistance and TGF-beta/FoxO signaling pathways (Supplementary Figure 2A). Platinum resistance is intrinsically coupled with homologous recombination proficiency, reinforcing the therapeutic vulnerability of SMC1B-deficient cells to DNA cross-linking

agents [25, 26]. Concurrently, the TGF-beta signaling axis is an established regulator of epithelial-mesenchymal transition and invasive phenotypes in PRAD [29], which harmonizes with our *in vitro* observations where SMC1B knockdown markedly impaired migration and invasion. Conversely, SMC1B-high tumors showed down-regulation of proteasome and branched-chain amino-acid degradation pathways, the latter consistent with the documented oncogenic role of BCAT1 in PRAD [30]. These observations support the view that SMC1B does not act in isolation but operates within a broader oncogenic network spanning DNA repair, growth-factor signaling, and metabolic reprogramming, all of which converge on the proliferative and invasive phenotypes confirmed in our cellular experiments.

In recent years, several studies have reported the value of SMC family proteins in tumor prognosis prediction [30-33], but none has systematically evaluated SMC1B in PRAD. We show that high SMC1B expression independently predicts shorter overall survival, and that integrating SMC1B into a nomogram and superior decision-curve net benefit relative to single-parameter models. Notably, SMC1B expression did not differ across T stages, suggesting that its prognostic value reflects intrinsic biological aggressiveness rather than local tumor invasion - a feature that is particularly attractive for stratifying patients with anatomically early-stage disease who nevertheless harbor high recurrence risk. It should be emphasized, however, that the discriminatory ability of SMC1B as a stand-alone prognostic marker is limited. Time-dependent ROC analysis yielded AUCs of only 0.64 (95% CI: 0.53-0.75), 0.60 (95% CI: 0.53-0.67), and 0.57 (95% CI: 0.48-0.65) for 1-, 3-, and 5-year overall survival, with a gradual downward trend and 95% confidence intervals approaching the non-informative threshold of 0.5 at later time points, indicating insufficient long-term predictive stability. Therefore, SMC1B is best regarded as a complementary biomarker that must be integrated with established clinicopathological variables (e.g., T stage, age, PSA, Gleason score) rather than used alone. Larger, prospective, multi-center cohorts combined with multi-marker panels will be required to formally validate the incremental prognostic value of SMC1B.

The development of single-cell RNA sequencing technology has provided unprecedented resolution to understand tumor heterogeneity. One study revealed the transformation of epithelial cells into mesenchymal-like cells during PRAD progression [34]. The normal prostate gland is composed of a bilayer structure of luminal and basal epithelial cells, and the basal cells have stem/progenitor cell properties [35]. A hallmark feature of PRAD is the loss of the basal cell layer, which is also an important basis for pathological diagnosis [36]. The reduced proportion of basal cells observed in this study is consistent with this pathological feature. Furthermore, the frequent communication between epithelial cells and basal cells may reflect the interaction between tumor cells and residual basal cells. Studies have found that there are subsets of cells with basal-like characteristics in PRAD, and these cells may be involved in the maintenance of tumor stemness and treatment resistance [18]. The strong communication strength between epithelial cells and endothelial cells suggests the importance of angiogenesis in PRAD progression. Tumor angiogenesis is one of the hallmark features of cancer, providing nutrition and oxygen supply for tumor growth and metastasis. Activation of VEGF signaling in PRAD is associated with disease progression and poor prognosis. Bevacizumab (VEGF inhibitor) combined with chemotherapy has shown some efficacy in castration-resistant PRAD [19]. In addition, sunitinib (a multitargeted tyrosine kinase inhibitor) has antitumor activity in metastatic PRAD [20]. The dense signaling between epithelial cells and T cells has important immunological implications. Although PRAD has less immune cell infiltration overall, epithelial cells can still interact with T cells through a variety of mechanisms. Tumor cells can express immune checkpoint ligands, such as PD-L1, to suppress T-cell activity. The expression of PD-L1 in PRAD is associated with immune cell infiltration and prognosis. On the other hand, tumor cells can also affect T cell recruitment through chemokine secretion [37]. As an important part of the tumor microenvironment, fibroblasts play a multifaceted role in tumor progression. Cancer-associated fibroblasts (CAFs) support tumor growth and invasion by secreting growth factors, cytokines and extracellular matrix remodeling proteins. CAFs in PRAD promote

tumor angiogenesis and metastasis. Studies have shown that PRAD-associated stromal cells can induce malignant transformation of normal prostate epithelial cells [38]. Although macrophages and mast cells are less prominent than the cell types mentioned above in the cell communication network in our study, they still play a role in the PRAD microenvironment. Mast cells are involved in tumor angiogenesis and immune regulation through the release of histamine, proteases, and cytokines. Mast cells promote angiogenesis and tumor growth in PRAD [39]. Taken together, the analysis of intercellular communication network reveals the complexity and dynamic nature of PRAD microenvironment. As the essential components of the tumor, epithelial cells not only have their own dysfunction, but also remodel the entire tumor ecosystem through signal interactions with a variety of microenvironment cells. The high expression and functional enrichment of SMC1B in epithelial cells may regulate the interaction between epithelial cells and the microenvironment by affecting the DNA repair ability, proliferation potential and signal transduction of epithelial cells, and ultimately promote tumor progression.

Several limitations should be acknowledged. First, SMC1B cis-eQTL instruments were obtained from the eQTLGen whole-blood dataset rather than prostate-specific tissue, chosen for its substantially larger sample size (n = 31,684) and greater statistical power than currently available prostate-tissue eQTL resources. Although cis-eQTL effects often show cross-tissue consistency, tissue-specific regulatory elements, chromatin accessibility, and transcription factor activity may affect their transferability to prostate tissue. Future studies incorporating prostate-specific eQTL (e.g., GTEx, PRACTICAL), together with multivariable MR accounting for correlated cohesin traits such as SMC1A and RAD21, would strengthen the causal inference. Second, although the MR-Egger intercept, Cochran's Q test, and leave-one-out analyses detected no directional pleiotropy or substantial heterogeneity, residual pleiotropy cannot be fully excluded, particularly given the potential regulation of neighbouring cohesin- or DNA-repair genes by variants within complex LD blocks at chromosome 22q13.31. Such effects may also act through broader cell-cycle, proliferative, or immune-compositional phenotypes that independently influence PRAD risk; integrative single-cell and spatial transcriptomics will help clarify the cell-type-specific regulation and microenvironmental interactions of SMC1B. Third, our mechanistic evidence for HR involvement remains correlative. Although γH2AX accumulation, RAD51 reduction, and downregulation of the BRCA1-PALB2-BRCA2 axis consistently point to HR impairment, DSB induction kinetics (IR, etoposide, or hydroxyurea), cytological RAD51 foci assays, and comet assays were not performed, and the regulatory hierarchy between SMC1B and the BRCA1-PALB2-BRCA2-RAD51 mediators was not resolved. Epistasis and ChIP-based experiments will be required to formally define SMC1B-deficient cells as HR-defective. Finally, the institutional validation cohort comprised only three paired tumour-normal specimens for RNA, protein, and IHC analyses, which should be regarded as preliminary exploratory evidence rather than definitive clinical validation; the small sample size precludes robust inference regarding effect size and inter-patient heterogeneity. A prospective, multicentre cohort of ≥ 50 paired specimens with complete clinicopathological annotation will be essential to validate SMC1B's prognostic value, and to assess whether SMC1B inhibition potentiates DNA damage-targeting therapies (PARP inhibitors, platinum agents, radiotherapy) through synthetic-lethal interactions, bridging the gap between genetic, mechanistic, and clinical evidence. In this expanded cohort, systematic semi-quantitative evaluation of IHC staining using the H-score method with independent assessment by two pathologists will be performed to formally correlate SMC1B protein expression with clinicopathological parameters.

Conclusion

This integrated study provides causal, cell-type-resolved, and in vitro evidence that elevated SMC1B expression is associated with aggressive prostate cancer phenotypes and perturbation of the BRCA1-PALB2-BRCA2-RAD51 homologous recombination mediator axis in malignant epithelial cells. SMC1B emerges as a promising candidate prognostic biomarker that integrates meaningfully into clinical nomograms, while its potential remains

a biologically coherent but currently unvalidated hypothesis that warrants prospective in vivo and clinical investigation.

Acknowledgements

We would like to express our sincere gratitude to all the participants for their contributions to this study.

Disclosure of conflict of interest

None.

Address correspondence to: Weiyang He, Department of Urology, The First Affiliated Hospital of Chongqing Medical University, No. 1 Youyi Road, Yuzhong District, Chongqing 400016, China. E-mail: gyfcqmn@163.com

References

[1] Guzman-Esquivel J, Murillo-Zamora E, Ortiz-Mesina M, Galvan-Salazar HR, De-Leon-Zaragoza L, Casarez-Price JC, Delgado-Enciso J and Delgado-Enciso I. Regional and national burden of prostate cancer: incidence, mortality, years of life lost, and disability-adjusted life years, in Mexico and Latin America from 1990 to 2019. Int Urol Nephrol 2023; 55: 2155-2160.

[2] Raychaudhuri R, Lin DW and Montgomery RB. Prostate cancer: a review. JAMA 2025; 333: 1433-1446.

[3] Ferlay J, Colombet M, Soerjomataram I, Parkin DM, Piñeros M, Znaor A and Bray F. Cancer statistics for the year 2020: an overview. Int J Cancer 2021; [Epub ahead of print].

[4] Cornford P, van den Bergh RCN, Briers E, Van den Broeck T, Cumberbatch MG, De Santis M, Fanti S, Fossati N, Gandaglia G, Gillessen S, Grivas N, Grummet J, Henry AM, der Kwast THV, Lam TB, Lardas M, Liew M, Mason MD, Moris L, Oprea-Lager DE, der Poel HGV, Rouvière O, Schoots IG, Tilki D, Wiegel T, Willemse PM and Mottet N. EAU-EANM-ESTRO-ESUR-SIOG guidelines on prostate cancer. part II-2020 update: treatment of relapsing and metastatic prostate cancer. Eur Urol 2021; 79: 263-282.

[5] Litwin MS and Tan HJ. The diagnosis and treatment of prostate cancer: a review. JAMA 2017; 317: 2532-2542.

[6] Sartor O and de Bono JS. Metastatic prostate cancer. N Engl J Med 2018; 378: 645-657.

[7] Uhlmann F. SMC complexes: from DNA to chromosomes. Nat Rev Mol Cell Biol 2016; 17: 399-412.

[8] Revenkova E, Herrmann K, Adelfalk C and Jessberger R. Oocyte cohesin expression restricted to predictyate stages provides full fertility and prevents aneuploidy. Curr Biol 2010; 20: 1529-1533.

[9] Li F, Wang Y, Wen M, Aizezi G, Yuan J, Zhou T and Shen G. NPHS2-6 drives cervical squamous cell carcinoma (CSCC) progression via hsa-miR-1323/SMC1B axis to activate PI3K-Akt pathway. Clin Transl Oncol 2024; 26: 245-259.

[10] Aoki H, Yamamoto E, Takasawa A, Niinuma T, Yamano HO, Harada T, Matsushita HO, Yoshikawa K, Takagi R, Harada E, Tanaka Y, Yoshida Y, Aoyama T, Eizuka M, Yorozu A, Kitajima H, Kai M, Sawada N, Sugai T, Nakase H and Suzuki H. Epigenetic silencing of SMOC1 in traditional serrated adenoma and colorectal cancer. Oncotarget 2017; 9: 4707-4721.

[11] Mannini L, Cucco F, Quarantotti V, Amato C, Tinti M, Tana L, Frattini A, Delia D, Krantz ID, Jessberger R and Musio A. SMC1B is present in mammalian somatic cells and interacts with mitotic cohesin proteins. Sci Rep 2015; 5: 18472.

[12] Davey Smith G and Hemani G. Mendelian randomization: genetic anchors for causal inference in epidemiological studies. Hum Mol Genet 2014; 23: R89-98.

[13] Emdin CA, Khera AV and Kathiresan S. Mendelian randomization. JAMA 2017; 318: 1925-1926.

[14] Burgess S, Small DS and Thompson SG. A review of instrumental variable estimators for Mendelian randomization. Stat Methods Med Res 2017; 26: 2333-2355.

[15] Yuan S, Carter P, Bruzelius M, Vithayathil M, Kar S, Mason AM, Lin A, Burgess S and Larsson SC. Effects of tumour necrosis factor on cardiovascular disease and cancer: a two-sample Mendelian randomization study. EBioMedicine 2020; 59: 102956.

[16] Dimou NL, Papadimitriou N, Gill D, Christakoudi S, Murphy N, Gunter MJ, Travis RC, Key TJ, Fortner RT, Haycock PC, Lewis SJ, Muir K, Martin RM and Tsilidis KK. Sex hormone binding globulin and risk of breast cancer: a Mendelian randomization study. Int J Epidemiol 2019; 48: 807-816.

[17] Puram SV, Tirosh I, Parikh AS, Patel AP, Yizhak K, Gillespie S, Rodman C, Luo CL, Mroz EA, Emerick KS, Deschler DG, Varvares MA, Mylvaganam R, Rozenblatt-Rosen O, Rocco JW, Faquin WC, Lin DT, Regev A and Bernstein BE. Single-cell transcriptomic analysis of primary and metastatic tumor ecosystems in head and neck cancer. Cell 2017; 171: 1611-1624, e1624.

[18] Dong B, Miao J, Wang Y, Luo W, Ji Z, Lai H, Zhang M, Cheng X, Wang J, Fang Y, Zhu HH, Chua CW, Fan L, Zhu Y, Pan J, Wang J, Xue W and Gao WQ. Single-cell analysis supports a luminal-neuroendocrine transdifferentiation in human prostate cancer. Commun Biol 2020; 3: 778.

[19] Chen S, Zhu G, Yang Y, Wang F, Xiao YT, Zhang N, Bian X, Zhu Y, Yu Y, Liu F, Dong K, Mariscal J, Liu Y, Soares F, Loo Yau H, Zhang B, Chen W, Wang C, Chen D, Guo Q, Yi Z, Liu M, Fraser M, De Carvalho DD, Boutros PC, Di Vizio D, Jiang Z, van der Kwast T, Berlin A, Wu S, Wang J, He HH and Ren S. Single-cell analysis reveals transcriptomic remodellings in distinct cell types that contribute to human prostate cancer progression. Nat Cell Biol 2021; 23: 87-98.

[20] Siciliano T, Simons IH, Beier AK, Ebersbach C, Aksoy C, Seed RI, Stope MB, Thomas C and Erb HHH. A systematic comparison of antiandrogens identifies androgen receptor protein stability as an indicator for treatment response. Life (Basel) 2021; 11: 874.

[21] Krais JJ, Wang Y, Patel P, Basu J, Bernhardy AJ and Johnson N. RNF168-mediated localization of BARD1 recruits the BRCA1-PALB2 complex to DNA damage. Nat Commun 2021; 12: 5016.

[22] Yarmolinsky J, Wade KH, Richmond RC, Langdon RJ, Bull CJ, Tilling KM, Relton CL, Lewis SJ, Davey Smith G and Martin RM. Causal inference in cancer epidemiology: what is the role of Mendelian randomization? Cancer Epidemiol Biomarkers Prev 2018; 27: 995-1010.

[23] Ibrahim A, Toss MS, Alsaleem M, Makhlouf S, Atallah N, Green AR and Rakha EA. Novel 2 gene signatures associated with breast cancer proliferation: insights from predictive differential gene expression analysis. Mod Pathol 2024; 37: 100403.

[24] Cheng H, Zhang N and Pati D. Cohesin subunit RAD21: from biology to disease. Gene 2020; 758: 144966.

[25] Valente D, Gentileschi MP, Guerrisi A, Bruzzaniti V, Morrone A, Soddu S and Verdina A. Factors to consider for the correct use of γH2AX in the evaluation of DNA double-strand breaks damage caused by ionizing radiation. Cancers (Basel) 2022; 14: 6204.

[26] Castroviejo-Bermejo M, Cruz C, Llop-Guevara A, Gutiérrez-Enríquez S, Ducy M, Ibrahim YH, Gris-Oliver A, Pellegrino B, Bruna A, Guzmán M, Rodríguez O, Grueso J, Bonache S, Moles-Fernández A, Villacampa G, Viaplana C, Gómez P, Vidal M, Peg V, Serres-Créixams X, Dellaire G, Simard J, Nuciforo P, Rubio IT, Dienstmann R, Barrett JC, Caldas C, Baselga J, Saura C, Cortés J, Déas O, Jonkers J, Masson JY, Cairo S, Judde JG, O'Connor MJ, Díez O, Balmaña J and Serra V. A RAD51 assay feasible in routine tumor samples calls PARP inhibitor response beyond BRCA mutation. EMBO Mol Med 2018; 10: e9172.

[27] Pritchard CC, Mateo J, Walsh MF, De Sarkar N, Abida W, Beltran H, Garofalo A, Gulati R, Carreira S, Eeles R, Elemento O, Rubin MA, Robinson D, Lonigro R, Hussain M, Chinnaiyan A, Vinson J, Filipenko J, Garraway L, Taplin ME, AlDubayan S, Han GC, Beightol M, Morrissey C, Nghiem B, Cheng HH, Montgomery B, Walsh T, Casadei S, Berger M, Zhang L, Zehir A, Vijai J, Scher HI, Sawyers C, Schultz N, Kantoff PW, Solit D, Robson M, Van Allen EM, Offit K, de Bono J and Nelson PS. Inherited DNA-repair gene mutations in men with metastatic prostate cancer. N Engl J Med 2016; 375: 443-453.

[28] Lozano R, Castro E, Aragón IM, Cendón Y, Cattrini C, López-Casas PP and Olmos D. Genetic aberrations in DNA repair pathways: a cornerstone of precision oncology in prostate cancer. Br J Cancer 2021; 124: 552-563.

[29] Zhang YF, Jiang R, Li JD, Zhang XY, Zhao P, He M, Zhang HZ, Sun LP, Shi DL, Zhang GX and Sun M. SMC1A knockdown induces growth suppression of human lung adenocarcinoma cells through G1/S cell cycle phase arrest and apoptosis pathways in vitro. Oncol Lett 2013; 5: 749-755.

[30] Wang XQ, Xu SW, Wang W, Piao SZ, Mao XL, Zhou XB, Wang Y, Wu WD, Ye LP and Li SW. Identification and validation of a novel DNA damage and DNA repair related genes based signature for colon cancer prognosis. Front Genet 2021; 12: 635863.

[31] Zhao Z, Wang X, Ding Y, Cao X and Zhang X. SMC4, a novel tumor prognostic marker and potential tumor therapeutic target. Front Oncol 2023; 13: 1117642.

[32] Yan W, Wang DD, Zhang HD, Huang J, Hou JC, Yang SJ, Zhang J, Lu L and Zhang Q. Expression profile and prognostic values of SMC family members in HCC. Medicine (Baltimore) 2022; 101: e31336.

[33] Nie H, Wu Y, Ou C and He X. Comprehensive analysis of SMC gene family prognostic value and immune infiltration in patients with pancreatic adenocarcinoma. Front Med (Lausanne) 2022; 9: 832312.

[34] Goncharov AP, Vashakidze N and Kharaishvili G. Epithelial-mesenchymal transition: a fundamental cellular and microenvironmental process in benign and malignant prostate pathologies. Biomedicines 2024; 12: 418.

[35] Pitzen SP and Dehm SM. Basal epithelial cells in prostate development, tumorigenesis, and cancer progression. Cell Cycle 2023; 22: 1303-1318.

[36] Triscott J, Lehner M, Benjak A, Reist M, Emerling BM, Ng CKY, de Brot S and Rubin MA. Loss of PI5P4Kα slows the progression of a Pten mutant basal cell model of prostate cancer. Mol Cancer Res 2025; 23: 33-45.

[37] Santoni M, Massari F, Cheng L, Cimadamore A, Scarpelli M, Montironi R and Lopez-Beltran A. PD-L1 inhibitors for the treatment of prostate cancer. Curr Drug Targets 2020; 21: 1558-1565.

[38] Atiya HI, Gorecki G, Garcia GL, Frisbie LG, Baruwal R and Coffman L. Stromal-modulated epithelial-to-mesenchymal transition in cancer cells. Biomolecules 2023; 13: 1604.

[39] Hempel Sullivan H, Maynard JP, Heaphy CM, Lu J, De Marzo AM, Lotan TL, Joshu CE and Sfanos KS. Differential mast cell phenotypes in benign versus cancer tissues and prostate cancer oncologic outcomes. J Pathol 2021; 253: 415-426.

Supplementary Table 1. Primer sequences used for qRT-PCR

Gene	Forward primer (5'→3')	Reverse primer (5'→3')
SMC1B	CGGCATCTATCCTGAGTACGA	TCCGTGTCTCTTGCTGCTTT
BRCA1	TGACACAGGTTTGGAGTATGC	GCACGGTTTCTGTAGCCCAT
PALB2	CCTCAGCTGTGAGGAGAAGG	GCTCTTTGGGCACGCTGAA
BRCA2	AAGCACTCCAGATGGCACAA	AATTCTTGACCAGGTGCGGT
RAD51	GCGACTCGCTGATGAGTTTG	CTGGTTGTTGATGCATGGGC
AR	CAGGTGTAGTGTGTGCTGGA	TGTAAGTTGCGGAAGCCAGG
KLK3	TTTCCAATGACGTGTGTGCG	CCAGAATCACCCGAGCAGG
GAPDH	AGGCCGGATGTGTTCGC	CAAATCCGTTGACTCCGACC

Supplementary Table 2. Heterogeneity test

Exposure	Outcome	Method	Q	Q_df	Q_pval
SMC1B	PRAD	MR Egger	12.84967728	8	0.11712747
SMC1B	PRAD	Inverse variance weighted	14.1541301	9	0.116947184

Supplementary Table 3. Pleiotropy test

Exposure	Outcome	egger_intercept	se	pval
SMC1B	PRAD	0.022054687	0.024473035	0.393811652

Supplementary Table 4. Steiger test

Exposure	Outcome	snp_r2.exposure	snp_r2.outcome	correct_causal_direction	steiger_pval
SMC1B	PRAD	0.03263482	0.000217061	TRUE	1.99E-127

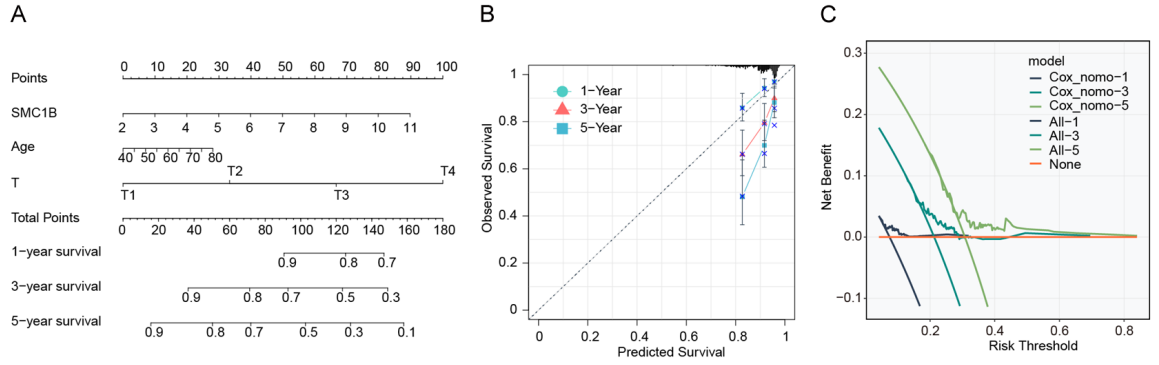

Supplementary Figure 1. Nomogram model. A. Prognostic prediction nomogram integrating SMC1B expression. B. Calibration curves of nomogram model. C. Decision curve analysis.

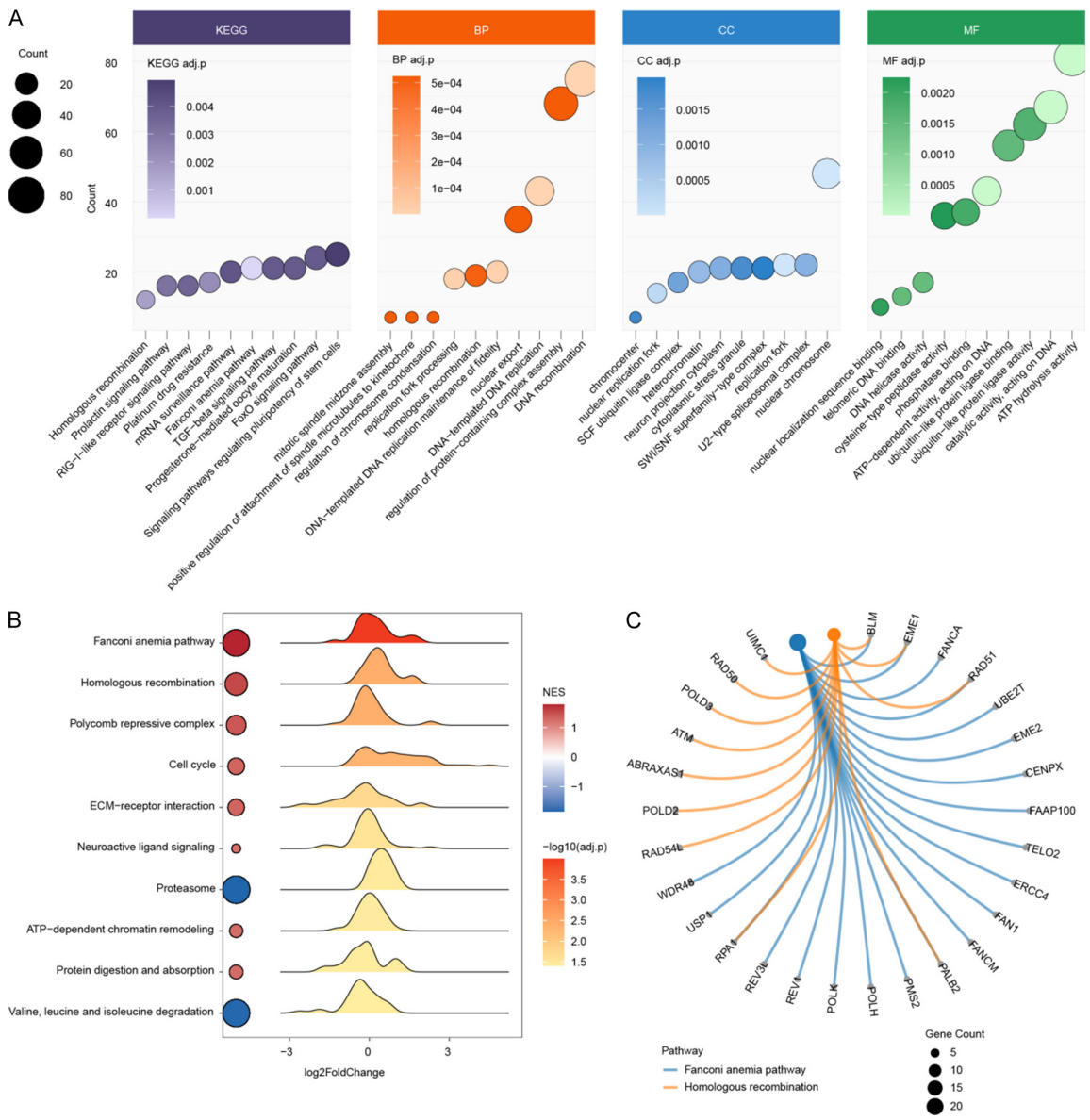

Supplementary Figure 2. Functional enrichment, GSEA validation, and core gene-pathway interactions of SMC1B co-expressed genes. A. Multi-panel bubble plot illustrating KEGG pathway and Gene Ontology (GO) enrichment across biological process (BP), cellular component (CC), and molecular function (MF) categories for the 1,970 SMC1B co-expressed candidate genes. Circle size indicates the count of enriched genes, and circle fill color represents the adjusted *P*-value (adj.p) within each facet. B. Ridgeline plot of single-gene GSEA displaying the distribution of core pathways validated between the SMC1B high- and low-expression groups. Point color indicates normalized enrichment score (NES; red for upregulation, blue for downregulation), and circle fill intensity corresponds to -log10(adj.p). C. Chord interaction network displaying the specific gene composition and pathway overlaps of the GSEA-validated Fanconi anemia pathway (blue arcs; 21 genes) and Homologous recombination pathway (orange arcs; 12 genes), highlighting the five shared key repair genes (BLM, EME1, PALB2, RAD51, and RPA1).

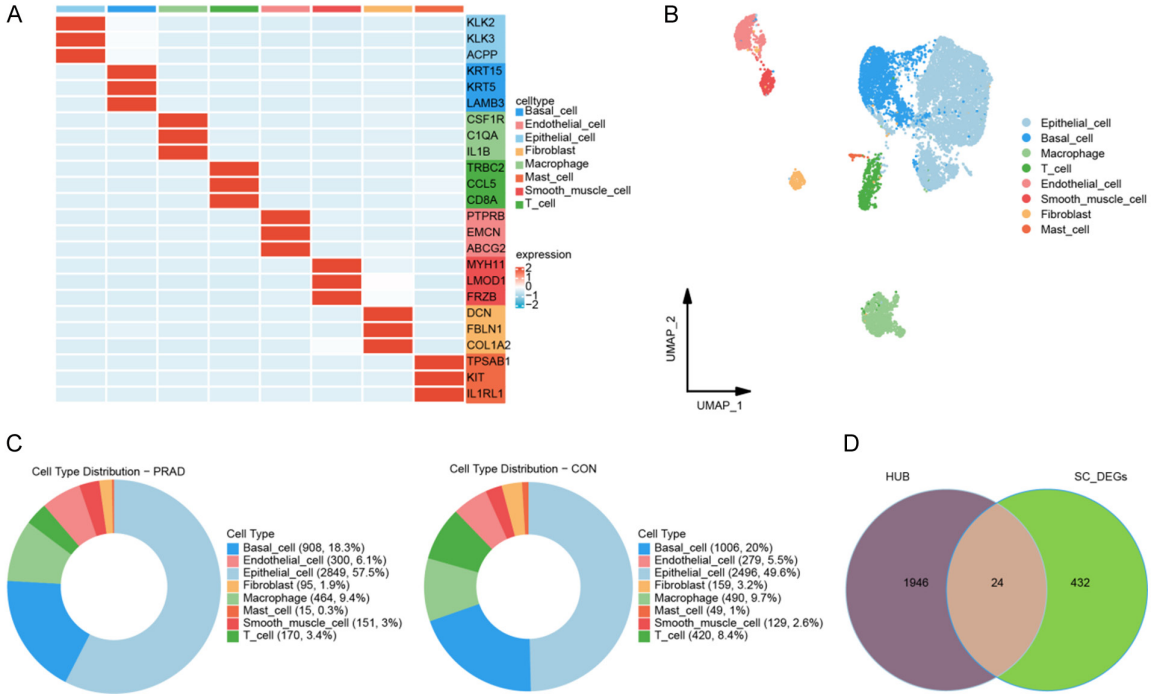

Supplementary Figure 3. Single-cell clustering, lineage annotation, microenvironmental composition, and functional gene set screening. A. Heatmap displaying expression profiles of canonical lineage marker genes across annotated cell types in the GSE176031 cohort. B. UMAP plot visualizing the eight major cell lineages: epithelial cells, basal cells, endothelial cells, fibroblasts, macrophages, smooth muscle cells, mast cells, and T cells. C. Donut charts depicting the relative cellular composition and proportional shifts between PRAD and CON tissues. D. Venn diagram illustrating the intersection between WGCNA co-expression hub genes (HUB, n = 1,970) and single-cell differentially expressed genes (SC_DEGs, n = 456), yielding the refined 24 core functional genes (comprising RAD51) of the SMC1B functional gene set.

Supplementary Table 5. Functional annotation and pathway assignment of the 24-gene SMC1B functional gene set in prostate cancer

Gene Symbol	Gene Full Name	Functional Category/Pathway	Biological Function in Genome Stability & DDR	Relevance in Prostate Cancer (PRAD) & Clinical Significance
RAD51	RAD51 Recombinase	Homologous Recombination (HR)/ Fanconi Anemia Pathway	Central recombinase that forms nucleoprotein filaments on ssDNA, driving strand invasion and homologous pairing during double-strand break (DSB) repair.	Key determinant of HR proficiency; overexpressed in aggressive PRAD and linked to castration resistance. Directly validated in vitro as downstream effector downregulated upon SMC1B knockdown.
ICA1	Islet Cell Autoantigen 1	Vesicle Trafficking/ Secretory Pathway	Interacts with BAR-domain proteins to regulate post-Golgi trafficking, neuroendocrine cargo transport, and cellular homeostasis.	Implicated in neuroendocrine differentiation, secretory activity, and aggressive clonal expansion in prostate cancer progression.
SPDEF	SAM Pointed Domain Containing ETS Transcription Factor	Epithelial Differentiation/Transcriptional Regulation	Prostate-specific ETS family transcription factor regulating luminal epithelial differentiation, cellular senescence, and stress-response networks.	Crucial biomarker of luminal prostate epithelial lineage; interacts with androgen receptor (AR) signaling to modulate metastasis and tumor cell plasticity.
DNPH1	2'-Deoxynucleoside 5'-Phosphate N-Hydrolase 1	Nucleotide Metabolism/Genomic Fidelity	Catabolizes cytotoxic/mutagenic nucleotide monophosphates (such as dUMP and halogenated dNTPs), safeguarding the nucleotide pool and genomic replication fidelity.	Overexpressed in proliferative epithelial malignancies; targeted to potentiate nucleotide-analog cytotoxicity and replication stress.
DVL1	Dishevelled Segment Polarity Protein 1	Wnt/Beta-Catenin Signaling/Cell Polarity	Core transducer of canonical and non-canonical Wnt signaling; links cell-surface frizzled receptors to downstream beta-catenin stabilization and spindle orientation.	Hyperactivated in PRAD; promotes epithelial-mesenchymal transition (EMT), cancer stem-like properties, bone metastasis, and therapy resistance.
MRPL24	Mitochondrial Ribosomal Protein L24	Mitochondrial Translation/Bioenergetics	Subunit of the 39S large mitochondrial ribosome; crucial for synthesizing oxidative phosphorylation complexes and maintaining mitochondrial membrane potential.	Upregulated to fuel the metabolic demands and rapid division of malignant prostate epithelial clones.
NIT2	Nitrilase Family Member 2	Metabolic Homeostasis/Amino Acid Metabolism	Omega-amidase that hydrolyzes alpha-ketoglutaramate; coordinates tumor cell nitrogen salvage and transamination homeostasis.	Associated with metabolic reprogramming and oxidative stress mitigation in prostate adenocarcinoma.
NME1	NME/NM23 Nucleoside Diphosphate Kinase 1	Nucleotide Pool Homeostasis/DNA Repair/Metastasis Suppression	Maintains cellular dNTP pools via nucleoside triphosphate synthesis; exhibits 3'-5' exonuclease activity and participates in DNA repair and genomic stability.	Modulates cell motility and metastatic dissemination; dysregulated expression correlates with disease recurrence and tumor progression.

NME3	NME/NM23 Nucleoside Diphosphate Kinase 3	Nucleotide Kinase/Genomic Stability	Participates in mitochondrial nucleotide homeostasis and early response to DNA double-strand breaks by interacting with repair machinery.	Supports survival of genotoxically stressed prostate tumor cells and maintains nucleotide availability for continuous DNA synthesis.
NPDC1	Neural Proliferation Differentiation And Control 1	Cell Cycle Control/ Proliferation	Interacts with E2F1 and cyclins to suppress uncontrolled cell cycle progression and promote neural/cellular differentiation.	Modulates G1/S transition and interacts with differentiation programs during prostate cancer dedifferentiation.
SLC25A39	Solute Carrier Family 25 Member 39	Mitochondrial Transport/Glutathione Homeostasis	Essential mitochondrial glutathione transporter; maintains intramitochondrial redox balance and iron-sulfur cluster assembly required for DNA repair enzymes.	Protects prostate carcinoma cells from oxidative stress and ferroptosis, sustaining aggressive tumor phenotype.
USE1	Unconventional SNARE In The ER 1	Endoplasmic Reticulum Transport/ Protein Homeostasis	Component of the ER-associated SNARE machinery; regulates retrograde Golgi-to-ER vesicle trafficking and protein folding stress.	Maintains secretory capability and buffers ER stress induced by rapid oncoprotein synthesis in PRAD epithelial cells.
EHBP1	EH Domain Binding Protein 1	Endocytic Trafficking/Cytoskeletal Dynamics	Links endocytic Rab-family GTPases with the actin cytoskeleton to regulate receptor endocytosis, sorting, and cell polarity.	Recognized prostate cancer risk locus (GWAS); modulates androgen receptor and EGFR recycling, promoting invasive behavior.
FAM13A	Family With Sequence Similarity 13 Member A	Rho-GTPase Signaling/Hypoxia Response	Acts as a RhoGAP activating GTPase-activating protein signaling; modulates beta-catenin degradation and cellular response to hypoxia.	Regulates tumor cell proliferation, survival in hypoxic prostate microenvironments, and epithelial plasticity.
GPD2	Glycerol-3-Phosphate Dehydrogenase 2 (Mitochondrial)	Glycerol-Phosphate Shuttle/Energy Metabolism	Transfers reducing equivalents from cytosolic NADH into the mitochondrial electron transport chain; essential for respiratory burst and ATP generation.	Drives metabolic remodeling, sustaining rapid proliferation and survival of malignant prostate epithelial cells.
ITGA6	Integrin Subunit Alpha 6 (CD49f)	Cell Adhesion/ Stemness/Extracellular Matrix Interaction	Forms laminin receptors (alpha6beta1/alpha6beta4); anchors cells to the basement membrane and regulates focal adhesion signaling and mechanical stress responses.	Classical prostate cancer stem cell marker; promotes invasive dissemination, perineural invasion, and cell-extracellular matrix cross-talk.
LAMC1	Laminin Subunit Gamma 1	Extracellular Matrix/Cell Migration & Invasion	Essential constituent of basement membrane laminins; regulates cell differentiation, migration, and structural maintenance of the glandular microenvironment.	Overexpressed in metastatic PRAD; coordinates CellChat-identified epithelial-stromal adhesion complexes to drive invasion.
LIMCH1	LIM And Calponin Homology Domains 1	Cytoskeleton Organization/Focal Adhesion Assembly	Actin-stress-fiber-associated protein that regulates non-muscle myosin II activity, focal adhesion stability, and cell motility.	Modulates cell migration and metastatic invasiveness; acts as a biomechanical regulator in prostate cancer dissemination.

LRRC8A	Leucine Rich Repeat Containing 8 VRAC Subunit A	Ion Channel/Volume Regulation & cGAMP Transport	Essential core subunit of the volume-regulated anion channel (VRAC); transports osmolytes, anticancer drugs (cisplatin), and immune cyclic dinucleotides (cGAMP).	Modulates platinum drug sensitivity, cell volume during migration, and antitumor immune surveillance in the tumor microenvironment.
NHLRC2	NHL Repeat Containing 2	Cytoskeletal Regulation/Cellular Stress Response	Involved in maintaining actin cytoskeleton integrity, multivesicular body formation, and protection against proteotoxic stress.	Supports survival and cytoskeletal remodeling in fast-dividing malignant prostate epithelial cells.
OCRL	OCRL Inositol Polyphosphate-5-Phosphatase	Phosphoinositide Signaling/Membrane Trafficking	Hydrolyzes PI(4,5)P2 to regulate early endosome trafficking, ciliogenesis, and cytokinesis during mitotic division.	Regulates receptor endocytosis (e.g., EGFR) and cell division fidelity in prostate cancer cells.
TBC1D14	TBC1 Domain Family Member 14	Autophagy Regulation/Rab-GAP Activity	Negative regulator of starvation-induced autophagy; controls membrane delivery from recycling endosomes to forming autophagosomes.	Coordinates autophagy flux and cellular survival under nutrient deprivation and metabolic stress in PRAD.
TMTC2	Transmembrane O-Mannosyltransferase Targeting Cadherins 2	Protein O-Mannosylation/Endoplasmic Reticulum	Transmembrane protein mediating O-mannosylation of cadherins in the ER; regulates ER calcium homeostasis and cell-cell adhesion.	Affects cadherin-mediated cell adhesion, glandular integrity, and invasive dissociation in prostate adenocarcinoma.
VTA1	Vesicle Trafficking 1 (ESCRT-III Associated)	ESCRT Machinery/Endosomal Sorting & Abscission	Stimulates the VPS4 ATPase in the ESCRT-III disassembly pathway; essential for multi-vesicular endosome sorting, membrane repair, and midbody abscission during cytokinesis.	Ensures complete cytokinesis and prevents genomic instability in rapidly dividing prostate cancer cells.

Notes: SC_DEGs, single-cell differentially expressed genes; WGCNA, weighted gene co-expression network analysis; DDR, DNA damage response; HR, homologous recombination; FA, Fanconi anemia; DSB, double-strand break; PRAD, prostate adenocarcinoma. RAD51 represents the central homologous recombination recombinase validated in vitro to confirm the downstream biological impact of siRNA-mediated SMC1B silencing.

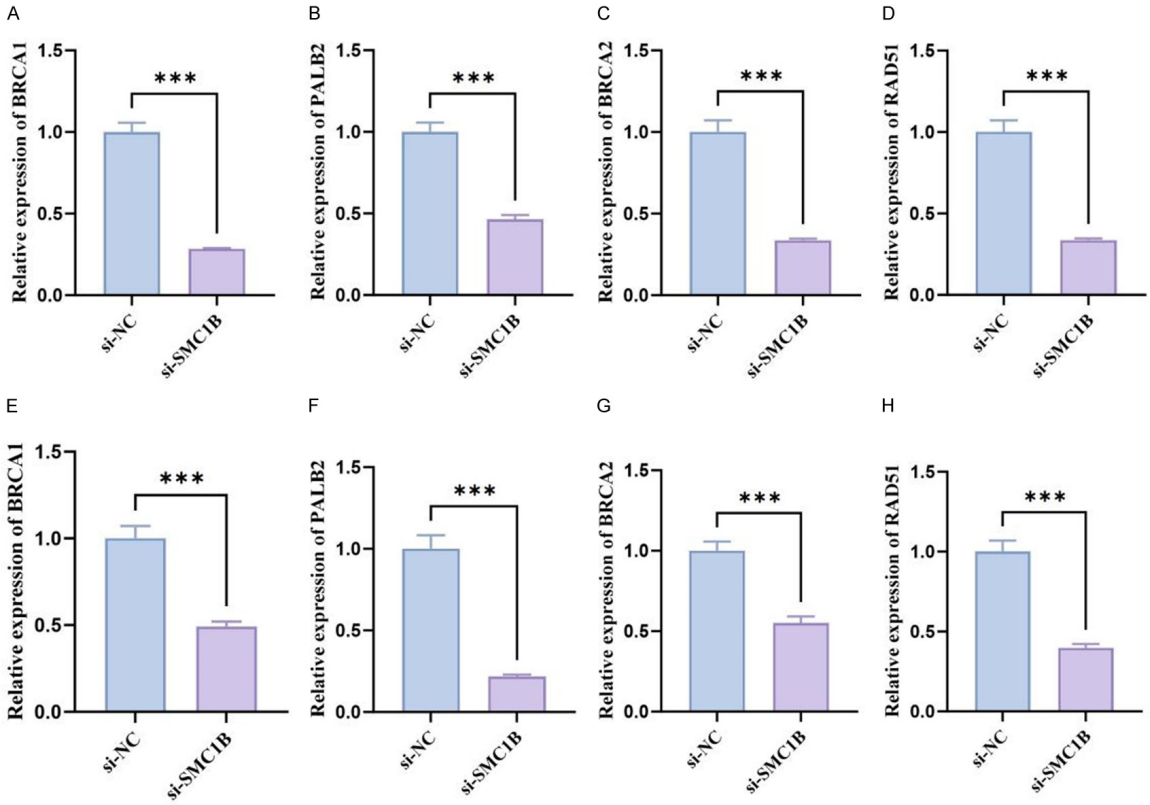

Supplementary Figure 4. SMC1B knockdown coordinately down-regulates BRCA1, PALB2, BRCA2, and RAD51 mRNA in PC-3 and LNCaP cells. (A-D) qRT-PCR quantification of BRCA1 (A), PALB2 (B), BRCA2 (C), and RAD51 (D) mRNA levels in si-NC- and si-SMC1B-transfected PC-3 cells. (E-H) qRT-PCR quantification of BRCA1 (E), PALB2 (F), BRCA2 (G), and RAD51 (H) mRNA levels in si-NC- and si-SMC1B-transfected LNCaP cells. mRNA levels were normalized to GAPDH and are presented relative to the si-NC group. Data are presented as mean ± SD (n = 3 biological replicates); ***P < 0.001 by unpaired two-tailed t-test.